

See discussions, stats, and author profiles for this publication at: <https://www.researchgate.net/publication/260407242>

Formic acid decomposition on Au catalysts: DFT, microkinetic modeling, and reaction kinetics experiments

ARTICLE in AICHE JOURNAL · APRIL 2014

Impact Factor: 2.75 · DOI: 10.1002/aic.14401

CITATIONS

8

READS

89

6 AUTHORS, INCLUDING:



Suyash Singh

University of Wisconsin–Madison

4 PUBLICATIONS 16 CITATIONS

SEE PROFILE



Sha Li

University of Wisconsin–Madison

4 PUBLICATIONS 30 CITATIONS

SEE PROFILE



Ronald Carrasquillo-Flores

University of Wisconsin–Madison

6 PUBLICATIONS 98 CITATIONS

SEE PROFILE



Ana C. Alba-Rubio

University of Toledo

18 PUBLICATIONS 271 CITATIONS

SEE PROFILE

Formic Acid Decomposition on Au Catalysts: DFT, Microkinetic Modeling, and Reaction Kinetics Experiments

Suyash Singh, Sha Li, Ronald Carrasquillo-Flores, Ana C. Alba-Rubio, James A. Dumesic, and Manos Mavrikakis

Dept. of Chemical and Biological Engineering, University of Wisconsin-Madison, Madison, WI 53706

DOI 10.1002/aic.14401

Published online February 27, 2014 in Wiley Online Library (wileyonlinelibrary.com)

A combined theoretical and experimental approach is presented that uses a comprehensive mean-field microkinetic model, reaction kinetics experiments, and scanning transmission electron microscopy imaging to unravel the reaction mechanism and provide insights into the nature of active sites for formic acid (HCOOH) decomposition on Au/SiC catalysts. All input parameters for the microkinetic model are derived from periodic, self-consistent, generalized gradient approximation (GGA-PW91) density functional theory calculations on the Au(111), Au(100), and Au(211) surfaces and are subsequently adjusted to describe the experimental HCOOH decomposition rate and selectivity data. It is shown that the HCOOH decomposition follows the formate (HCOO) mediated path, with 100% selectivity toward the dehydrogenation products ($\text{CO}_2 + \text{H}_2$) under all reaction conditions. An analysis of the kinetic parameters suggests that an Au surface in which the coordination number of surface Au atoms is ≤ 4 may provide a better model for the active site of HCOOH decomposition on these specific supported Au catalysts. © 2014 American Institute of Chemical Engineers AIChE J, 60: 1303–1319, 2014

Keywords: catalysis, formic acid decomposition, active sites, density functional theory, microkinetic modeling

Introduction

The effective utilization of renewable energy carriers produced from biomass-based resources is one of the key challenges in the transition toward a sustainable energy future.^{1,2} Formic acid (FA, HCOOH) is a major byproduct in biomass processing,³ and it has attracted significant attention as a potential hydrogen-carrier material.^{4–9} As a hydrogen-carrier, FA can be oxidized in direct formic acid fuel cells (DFAFCs).¹⁰ When generated as an equimolar by-product of levulinic acid^{11–13} production from cellulosic biomass, FA can be used for *in situ* harvesting H_2 that can then be utilized for the hydrogenation of levulinic acid to gamma-valerolactone,¹⁴ thereby eliminating the need of an external hydrogen source in the production of this key biofuel precursor.^{15,16} Also, as the simplest carboxylic acid, FA has for long been considered a paradigmatic molecule in homogeneous and heterogeneous catalysis, and surface science studies, to probe the reactivity on metals,^{17–26} metal carbides,^{27–29} and metal oxides^{30–35} specifically for deoxygenation of more complex carboxylic acids, which is a critical step in the selective upgrading of biomass derived platform molecules to fuels. Hence, our motivation for studying the FA decomposition reaction is based on (1) its potential application as a promising liquid hydrogen carrier for *in situ* hydrogen pro-

duction and (2) its suitability as a fundamental probe molecule for understanding the reactivity of carboxylic acids on metal catalysts, and using this information to design improved catalysts for effective deoxygenation of these functional groups. FA decomposition can take place via two parallel pathways involving dehydrogenation or dehydration reactions, which are linked by the water gas shift (WGS)^{36–38} reaction. In the broader context of FA decomposition on transition metals, steering selectivity toward production of carbon dioxide (CO_2) + H_2 (dehydrogenation), rather than carbon monoxide (CO) + H_2O (dehydration) presents an important selectivity challenge in this catalytic chemistry. Even though the dehydration products can be transformed to CO_2 and H_2 via the WGS reaction, forming the dehydration products may lead to partial poisoning of catalytic sites by CO , thereby limiting the efficiency of the overall catalysis. Accordingly, supported Pt catalysts have frequently been suggested to be the most active catalysts for selective FA dehydrogenation, and for this reason, they find widespread applications as anodes for DFAFCs.^{39–45} Yet, there exist major obstacles in using Pt-based catalysts as electrode materials and as FA decomposition catalysts, because of the proneness of Pt to CO poisoning^{46–48} and its dissolution under operating conditions in fuel cells.

Gold, conversely, is not hindered by CO poisoning under most reaction conditions. Ever since Haruta et al.⁴⁹ and Hutchings⁵⁰ first predicted Au to be an extraordinary catalyst for CO oxidation and ethylene hydrochlorination reactions, there has been an overwhelming interest in exploring the application of supported Au catalysts in both homogeneous and heterogeneous catalysis.^{51–59} More recently, Au has

Additional Supporting Information may be found in the online version of this article.

Suyash Singh and Sha Li contributed equally to this work.

Corresponding concerning this article should be addressed to M. Mavrikakis at mannos@engr.wisc.edu.

© 2014 American Institute of Chemical Engineers

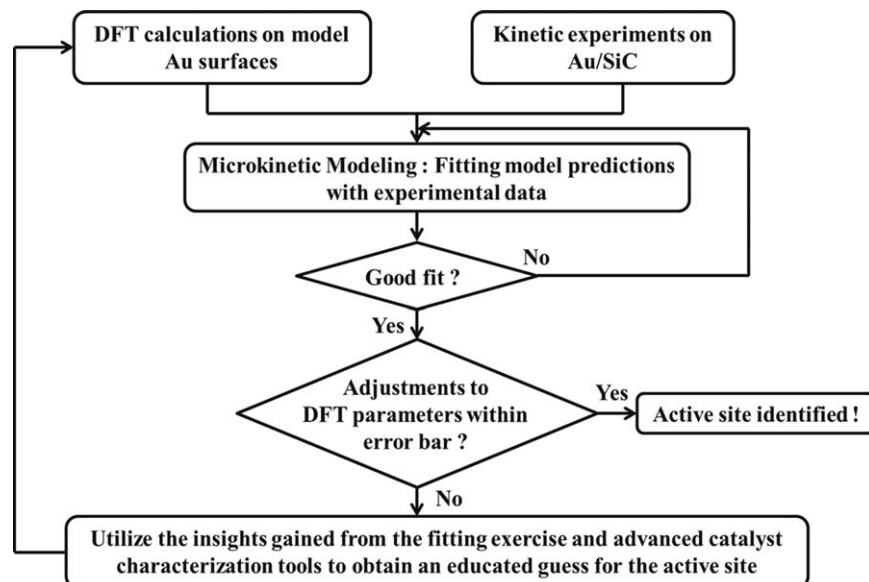


Figure 1. Flow chart for the identification of active sites for FA decomposition on Au/SiC.

been studied as a catalyst for FA decomposition.⁶⁰ In particular, Ojeda and Iglesia⁶¹ studied the FA decomposition on supported Au catalysts and showed that the turnover frequencies (TOFs) on well-dispersed Au catalysts were higher than those on Pt catalysts. They proposed that this unprecedented activity on Au catalysts arises from small Au clusters, most likely undetected in transmission electron microscopy (TEM) micrographs. More recently, Gazsi et al.⁶² performed vapor-phase experiments to study the effect of supports on the selectivity of FA decomposition to the dehydration and dehydrogenation products, and they confirmed the high activity of Au nanoparticles supported on a wide range of porous and nonporous supports. Although these experimental studies

shed light on the possible nature of active sites on Au catalysts, a molecular level understanding of this reaction mechanism is still lacking. In this article, we develop an integrated approach (Figure 1) by combining state-of-the-art density functional theory (DFT) with reactivity experiments and microkinetic modeling that can shed additional light into the reaction mechanism and the nature of active sites on Au catalysts.⁶³ In particular, we choose Au(111), Au(100), and Au(211) model surfaces for our DFT calculations to derive initial guesses for the surface reaction energetics needed for our microkinetic model. We then develop a comprehensive mean-field microkinetic model including all elementary steps investigated by our DFT calculations. Comparisons between

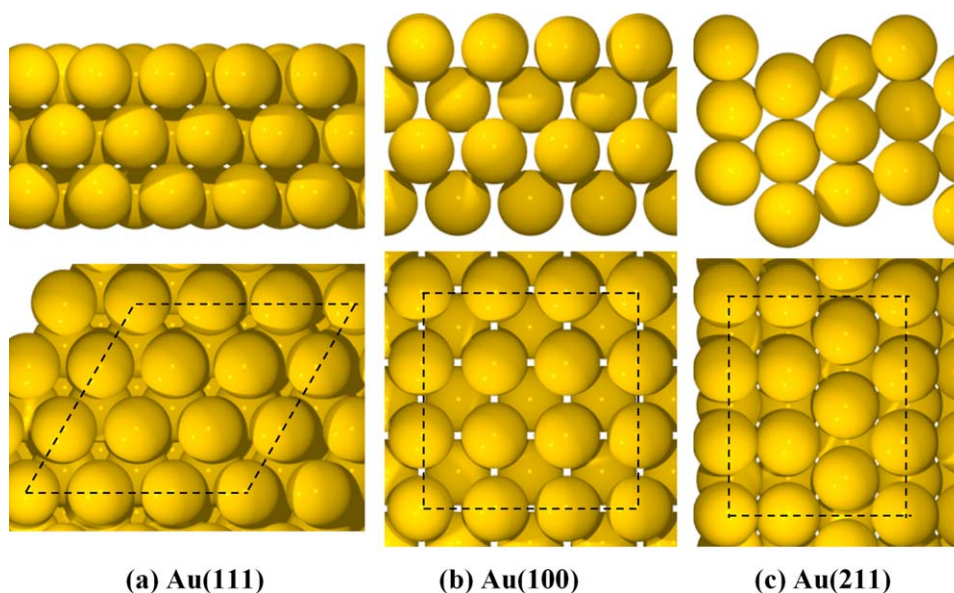


Figure 2. Side and top views of the three model Au surfaces used in this study: (a) Au(111), (b) Au(100), and (c) Au(211).

Dotted black lines in the top view indicate the unit cell on each surface. [Color figure can be viewed in the online issue, which is available at wileyonlinelibrary.com.]

microkinetic modeling reaction rates and reaction orders with the experimental results provide critical insights for the nature of the active site on Au/SiC catalysts for FA decomposition.

Methods

Density functional theory

All calculations were performed using the DACAPO total energy code.^{64,65} The Au catalyst was modeled by the (111), (100), and (211) facets of the fcc bulk crystalline structure of Au metal (Figure 2).

The Au(111) surface was modeled by a three-layer slab with a $p(3 \times 3)$ unit cell, corresponding to 1/9 monolayer (ML) coverage for a single adsorbate in the unit cell, periodically repeated in a super cell geometry with five equivalent layers of vacuum between any two successive metal slabs. All the Au atoms in this model surface were kept fixed in their bulk truncated positions, as our systematic investigations showed that surface relaxation does not have a significant effect on the energetics for this system. The super cell used to model the Au(100) facet consists of a $p(3 \times 3)$ unit cell with four layers of metal atoms, top two of which were allowed to relax, and five equivalent layers of vacuum spacing separating the periodic slab images. The Au(211) slab was constructed by a 1×3 unit cell and consisted of nine Au layers (having terrace three atoms deep and three atoms wide). Successive slabs were separated by a vacuum equivalent to 12 such Au(211) layers. Adsorption was allowed on only one of the two exposed surfaces for all three slabs, and the electrostatic potential was adjusted accordingly.^{66,67}

The surface Brillouin zone of (111) slabs was sampled at 18 special Chadi–Cohen⁶⁸ k-points, whereas that for the (100) and (211) slabs were sampled using a $4 \times 4 \times 1$ Monkhorst–Pack⁶⁹ k-point mesh. Ionic cores were described by ultrasoft Vanderbilt pseudopotentials⁷⁰ and the Kohn–Sham one-electron valence states were expanded in a basis of plane waves below a kinetic energy of 25 Ry. The exchange–correlation energy and potential were described self-consistently using the generalized gradient approximation (GGA-PW91).^{71,72} The electron density was determined by iterative diagonalization of the Kohn–Sham Hamiltonian, Fermi population of the Kohn–Sham states ($k_B T = 0.1$ eV), and Pulay mixing of the resulting electronic density.⁷³ The total energies were then extrapolated to $k_B T = 0$ eV. The calculated equilibrium lattice constant for bulk Au was found to be 4.18 Å, in reasonable agreement with the experimental value (4.08 Å).⁷⁴

The binding energies (BEs) were calculated with respect to the total energy of the clean slabs (E_{slab}) and the corresponding adsorbates in the gas phase ($E_{\text{adsorbate, gas-phase}}$), that is, $\text{BE}_{\text{adsorbate}} = E_{\text{total}} - E_{\text{slab}} - E_{\text{adsorbate, gas-phase}}$. In the discussion of the DFT results, we refer to electronic energy values including the zero-point energy (ZPE) corrections unless otherwise noted.

The minimum energy pathways and activation energy barriers for all elementary steps were determined using the climbing image nudged elastic band method.^{75,76} The minimum energy path for each elementary step was discretized with at least seven images, in addition to the initial and final states. A vibrational frequency analysis⁷⁷ was performed to confirm the true nature of the saddle point by identifying a single imaginary frequency along the reaction coordinate.

The frequencies were calculated using the harmonic oscillator assumption by diagonalization of the mass-weighted Hessian matrix in internal coordinates.⁷⁷

Experiments

Catalyst Preparation. SiC was chosen as the preferred support for our reaction kinetics experiments because (1) it is an inert support that does not contribute to the overall reaction rate and (2) it results in a clear contrast for Au atoms and clusters in the scanning transmission electron microscopy (STEM) micrographs, due to the large difference in the scattering potentials of the metal and the support. A 1 wt % Au/SiC catalyst was prepared by the deposition-precipitation method. 2.0 g of dry acid-treated silicon carbide was dispersed in 100 mL of a 1 mM chloroauric acid (Sigma-Aldrich) solution at room temperature. The pH of the mix was adjusted to 9 by drop-wise addition of 2.5 M ammonium hydroxide (Sigma-Aldrich). The mixture was aged for 6 h under vigorous stirring at room temperature and was then filtered and washed with deionized water to remove chlorine ions. The sample was dried overnight at 373 K. The dried catalyst was reduced *in situ*, prior to the reaction at a temperature between 623 and 773 K (with a heating rate of 0.5 K min^{-1}) under pure hydrogen flow (30 cm^3 Standard Temperature and Pressure (STP) min^{-1}) for 4 h. Catalyst reductions at temperatures above 773 K (and up to 1073 K) were performed in a quartz flow-through cell under the same operating conditions.

Reactivity Measurements. Gas phase FA decomposition studies were conducted in a fixed-bed down-flow reactor containing 120 mg of catalyst mixed with silica chips in a 1/2-inch outer diameter stainless steel tube. The temperature was measured using a K-type thermocouple attached to the outside of the reactor. The temperature of the reactor was adjusted using a furnace connected to a variable autotransformer power source controlled with a temperature controller. The total pressure in the reactor was maintained at 1 atm, and the partial pressures of the gases were controlled by adjusting the flow rates at the reactor inlet. The flow rates of all gases were fixed using calibrated mass-flow meters, and the total inlet flow rate was maintained at 100 mL min^{-1} for all experimental runs. An inlet composition between 0–6% of H_2 , 0–6% of CO_2 , and 1–4% of FA was used, with the balance consisting of helium. The gases were used as provided, with a purity of 99.99%. Liquid FA (Sigma-Aldrich) was delivered to the reactor system at room temperature using a syringe pump (Harvard Apparatus) and vaporized at the reactor inlet. The feed and effluent gases were analyzed using gas chromatography (with a Thermal Conductivity Detector (TCD)). All the experimental rates reported in this study are based on FA converted, which is equal to the amount of CO_2 produced, as no measurable amount of CO is formed under any experimental condition. To ensure this, the TCD used to analyze CO in the effluent gas mixture was first calibrated using commercial CO gas mixtures with known concentrations. Control experiments with only the SiC support in the reactor provided signals that corresponded to a concentration of 24 ± 1 ppm of CO. The CO concentrations that were obtained during our kinetic experiments under all reaction conditions were found to be very close to this value (max = 27.0 ppm, min = 23.2 ppm, average over all the runs = 25.1 ± 2 ppm). The carbon balance was verified for all experimental runs and was found to

Table 1. Calculated PW91 Binding Energies (BEs) of Adsorbed Species and their Preferred Adsorption Sites on Au(111), Au(100), and Au(211)

Species	Au(111)		Au(100)		Au(211)	
	Adsorption Site	BE (eV)	Adsorption Site	BE (eV)	Adsorption Site	BE (eV)
H*	fcc	−1.90	bridge	−2.06	bridge	−2.11
O*	fcc	−2.41	hollow	−2.69	bridge	−2.80
OH*	bridge	−1.36	bridge	−1.96	bridge	−2.07
H ₂ O*	top	−0.10	top	−0.14	off-top	−0.20
CO*	top	−0.21	bridge	−0.62	bridge	−0.67
CO ₂ *	physisorbed	−0.02	physisorbed	−0.02	physisorbed	−0.05
HCO*	top	−1.05	top	−1.26	top	−1.38
HCOO**	top–top	−1.69	top–top	−2.02	top–top	−2.19
COOH*	top	−1.27	top	−1.48	top	−1.58
COOH _{cis} *	top	−1.22	top	−1.48	top	−1.59
HCOOH*	top	−0.10	top	−0.16	top	−0.21

Zero of the energy scale is the slab and the gas-phase species at infinite separation from each other.

be in the range of 98.9–99.9%. Conversions were maintained below 20% to achieve differential reactor operation. To determine the apparent activation energy barrier, the temperature was varied over a range of 50 K, with the concentrations kept at standard conditions. The apparent reaction orders with respect to reactants and products were determined by varying one gas concentration at a time.

Characterization by STEM. The particle-size distributions were determined from STEM images. STEM characterization was performed using a FEI Titan STEM with CEOS probe aberration corrector operated at 200 kV with spatial resolution of <0.1 nm. For imaging, a high-angle annular dark-field (HAADF) Z-contrast STEM was used, with HAADF detector angle ranging from 54 to 270 mrad, probe convergence angle of 24.5 mrad, and probe current of ~25 pA. To prepare samples for STEM, the catalyst samples were first suspended in ethanol, ultrasonicated for 5 min, and then deposited onto a ~5 nm thick Si window TEM grids. STEM samples were plasma cleaned for 10 min with 20% O₂ + 80% Ar gas immediately before loading into the microscope.

The particle-size distributions of the Au/SiC catalysts were calculated from the acquired STEM images. From the particle-size distributions, the number average Au particle sizes were determined using the relation $d = \sum_i d_i / n$, where d_i is the particle diameter of each Au particle, n is the total number of Au particles counted from the STEM images of a given sample (Table 6), and the summation was performed over all the particles that were identified in the STEM images.

Microkinetic modeling

A mean-field microkinetic model for FA decomposition was developed on the basis of 17 elementary steps, including some steps that are in common with the WGS reaction. The initial estimates for the ZPE-corrected BEs and activation energy barriers were derived from DFT calculations and were later adjusted to reproduce the experimental kinetic dataset collected on the Au/SiC catalysts. Entropies of adsorbed intermediates and pre-exponential factors were determined from the DFT-calculated vibrational frequencies following a procedure described elsewhere.⁷⁸ Lateral adsorbate–adsorbate interactions were neglected and all the BEs and activation energy barriers (E_A s) were assumed to be coverage independent. This assumption is reasonable as we

expect surface coverages to be low under our experimental conditions. The maximum surface coverage was restricted to 1 ML and multilayer adsorption was not considered. We assumed that all species occupy exactly one site on the surface, except for the bidentate formate (HCOO), which blocks two surface sites. Given the geometry of the reactor used in our experiments, the reactor was modeled as a plug-flow reactor. Hence, our reactor model comprised of five differential equations for the gaseous flow rate along the reactor length, eight steady-state algebraic equations for the fractional surface coverages of reaction intermediates, and one site-balance equation. Further details of our model formulation can be found in our previous work.^{63,78,79}

Results and Discussion

To develop a comprehensive mean-field microkinetic model that would enable us to study the structure sensitivity of this reaction on Au surfaces, we have rigorously studied the properties of five closed-shell species and eight reaction intermediates, as well as the reaction energetics of 17 elementary steps, on the Au(111), Au(100), and Au(211) facets using first principles DFT calculations. We first present the results from our DFT calculations; followed by the results from our attempts to fit the microkinetic model predicted rates and selectivities to the experimentally measured reaction kinetics data.

Structure and adsorption thermochemistry of reaction intermediates

The BEs and preferred adsorption sites of surface species involved in this reaction network on the three Au facets studied are summarized in Table 1. More detailed information on adsorbed states, including vibrational frequencies of surface intermediates and gas-phase species can be found in Supporting Information (Table S1–S4).

The following description focuses primarily on the most favorable binding configurations for the adsorbates. Schematic representations for these configurations are shown in Figures 3–6. In this discussion, and throughout the text, (g) stands for “gas-phase species” and each “*” represents a single surface site occupied by the corresponding adsorbate. Wherever available, the previously reported literature values (as obtained using DFT) for the BEs of surface species and activation energy barriers (E_A) of elementary steps are reported in parenthesis next to our DFT derived numbers.

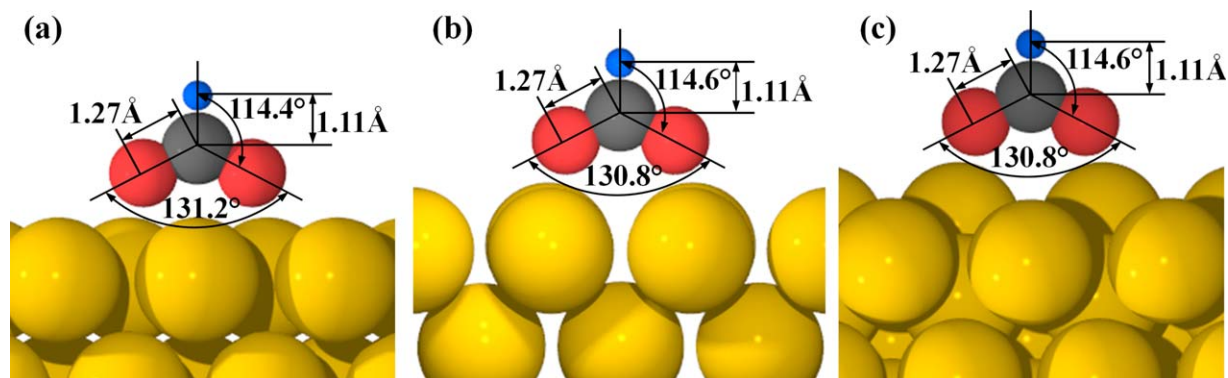


Figure 3. Most stable configurations of Formate (HCOO) intermediate on (a) Au(111), (b) Au(100), and (c) Au(211).

[Color figure can be viewed in the online issue, which is available at wileyonlinelibrary.com.]

All the closed-shell species involved in this reaction network, with the exception of CO, are found to be weakly bound to all three Au facets studied. They exhibit weak preference for their most stable binding configurations, as evidenced by the near degeneracy of their several adsorption states. Our calculations do not take into account the long-range interactions, such as van der Waals forces,^{80,81} which may contribute an additional stabilization of ~ 0.1 – 0.2 eV per carbon atom. The absolute magnitude of the BEs of surface species on the three Au surfaces were observed to decrease in the general order: Au(211) > Au(100) > Au(111), in agreement with the general notion that adsorbates tend to exhibit stronger binding to more open facets.⁸²

FA exhibits two distinct stable configurations: one in which all atoms of the HCOOH* molecule lie within a plane

perpendicular to the surface (HCOOH*), and another one in which this plane is parallel to the surface (HCOOHpa*). The latter orientation was found to adsorb with practically zero BE on all three surfaces. HCOOH* binds to the three facets via its carbonyl O atom on a top site with the O–H and C–H bonds pointing toward and away from the surface, respectively, and has a BE of -0.10 eV (-0.15 eV⁸³), -0.16 eV (-0.19 eV⁸⁴), and -0.21 eV on Au(111), Au(100), and Au(211), respectively. Formate has long been proposed as one of the key reaction intermediates in FA decomposition and has also been frequently cited as a possible intermediate in WGS^{85–87} and methanol synthesis^{88–90} reactions. As a result, it has received much scientific attention,^{35,61,91–96} both in the experimental and theoretical literature. Our DFT calculations indicate that HCOO** binds on all three Au facets in a

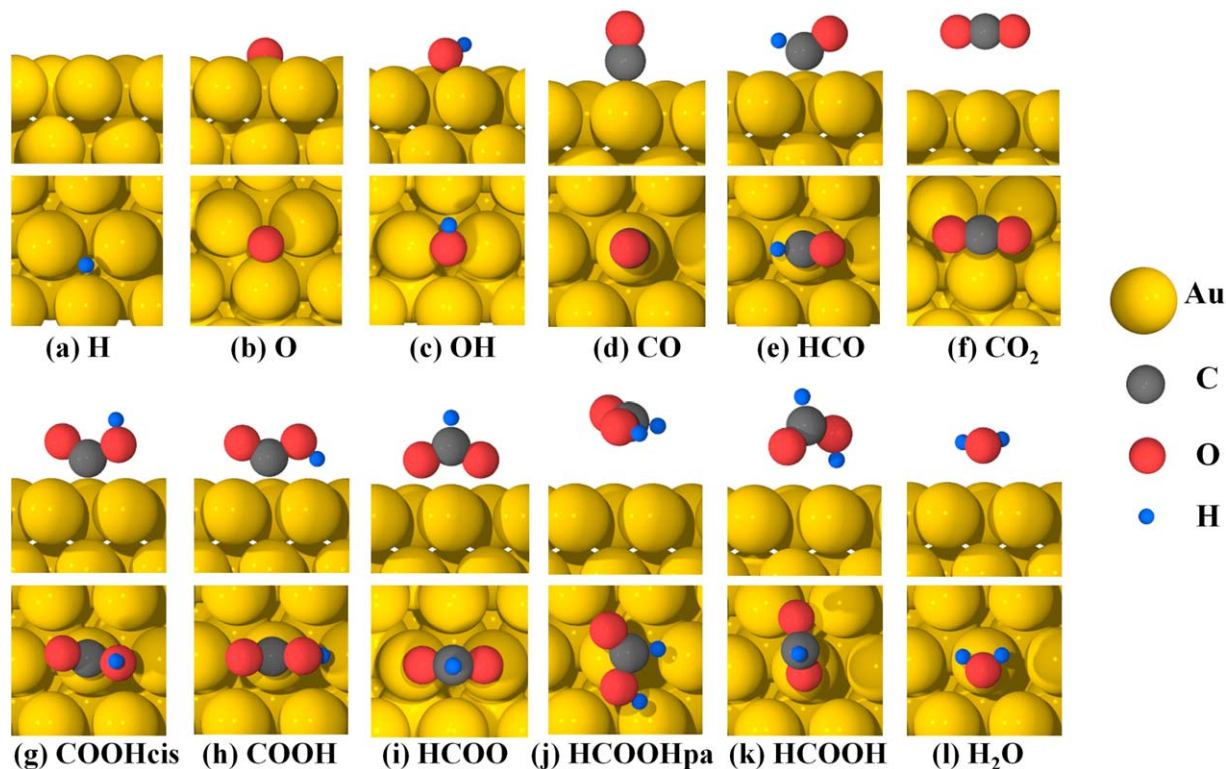


Figure 4. Most stable configurations of FA decomposition intermediates on Au(111) (top panel represents cross-sectional view; bottom panel represents top view).

[Color figure can be viewed in the online issue, which is available at wileyonlinelibrary.com.]

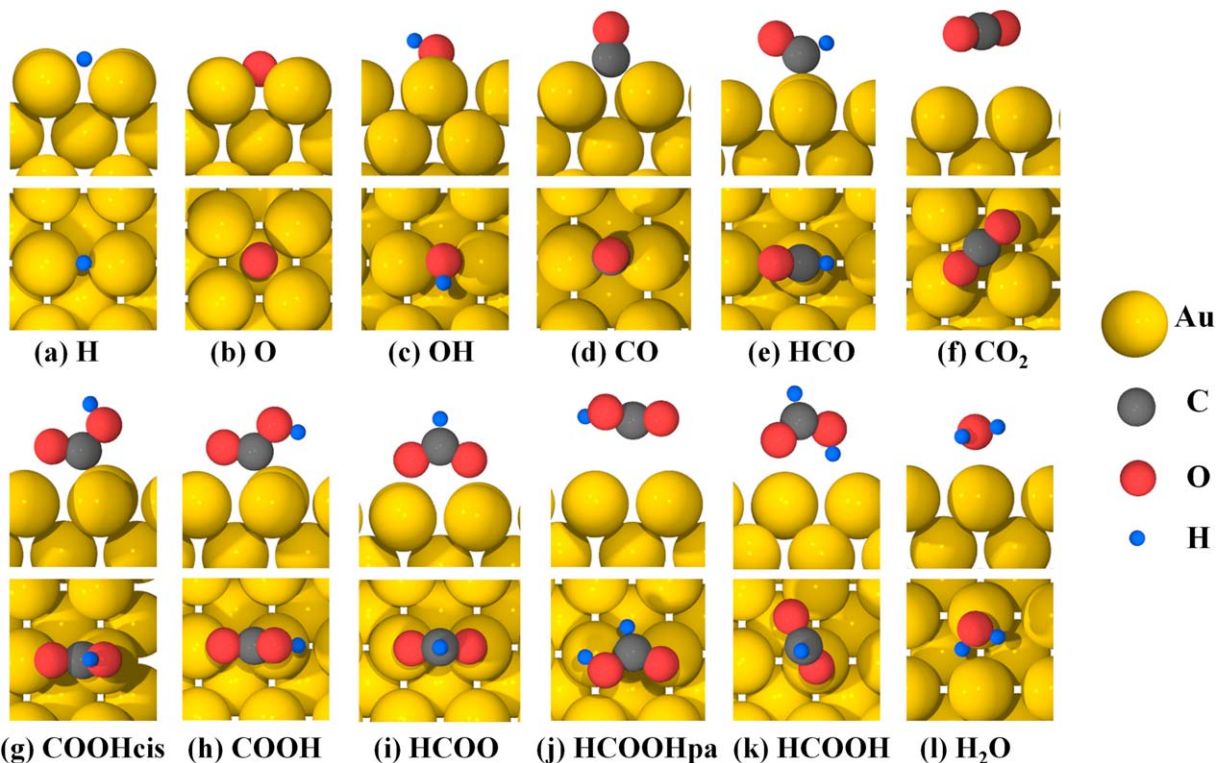


Figure 5. Most stable configurations of FA decomposition intermediates on Au(100) (top panel represents cross sectional view; bottom panel represents top view).

[Color figure can be viewed in the online issue, which is available at wileyonlinelibrary.com.]

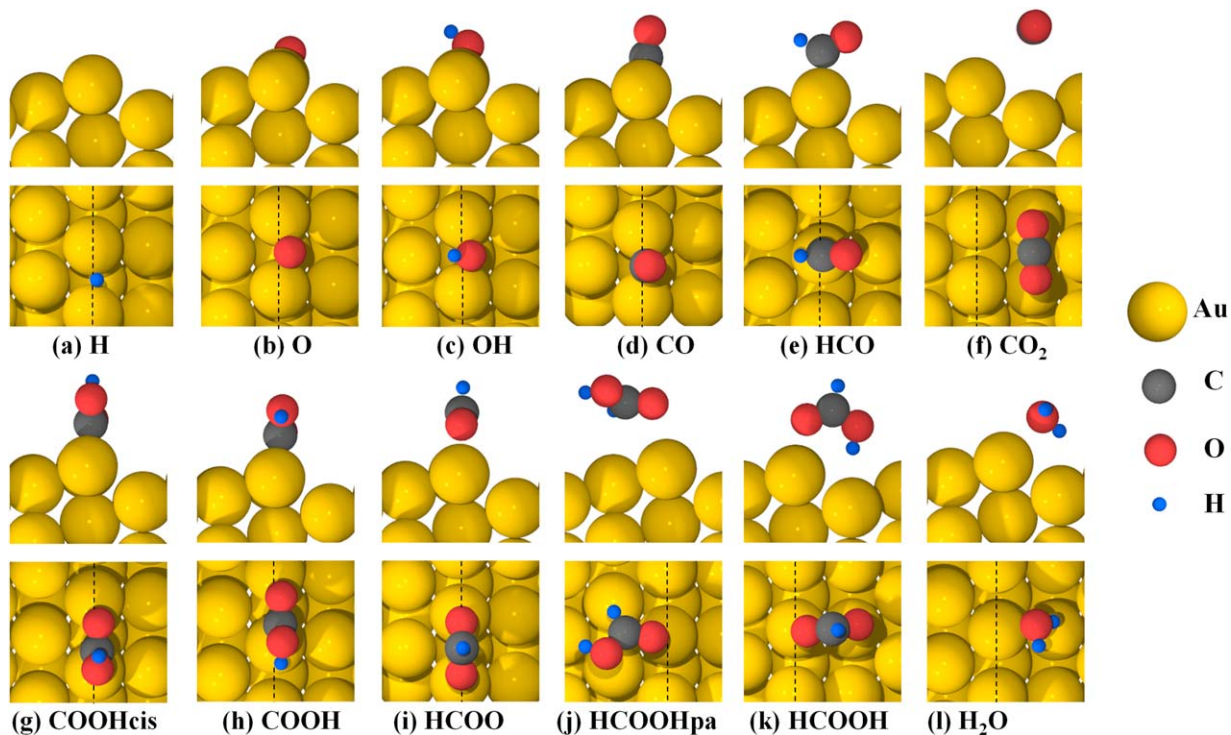


Figure 6. Most stable configurations of FA decomposition intermediates on Au(211) (top panel represents cross-sectional view; bottom panel represents top view; dotted black lines in the top view denote the step edge of Au(211) surface).

[Color figure can be viewed in the online issue, which is available at wileyonlinelibrary.com.]

Table 2. PW91 Reaction Energies (ΔE) and Activation Energy Barriers (E_A) for the Elementary Steps Considered in the HCOOH Decomposition Reaction Network on Au(111), Au(100), and Au(211) Surfaces

#	Reaction	Au(111)		Au(100)		Au(211)	
		ΔE (eV)	E_A (eV)	ΔE (eV)	E_A (eV)	ΔE (eV)	E_A (eV)
1	$\text{HCOOH} + * \leftrightarrow \text{HCOOH}^*$	-0.10		-0.16		-0.21	
2	$\text{HCOOH}^* \leftrightarrow \text{HCOOHpa}^*$	0.24	0.55	0.29	0.59	0.26	0.63
3	$\text{HCOOH}^* + 2* \leftrightarrow \text{HCOO}^{**} + \text{H}^*$	0.86	1.29	0.42	0.87	0.26	0.98
4	$\text{HCOOHpa}^* + * \leftrightarrow \text{COOH}^* + \text{H}^*$	0.80	1.22	0.44	0.83	0.37	0.87
5	$\text{HCOOH}^* + * \leftrightarrow \text{HCO}^* + \text{OH}^*$	2.32	2.16	1.57	1.91	1.38	1.74
6	$\text{HCOO}^{**} \leftrightarrow \text{CO}_2^* + \text{H}^*$	-0.35	0.80	-0.17	0.84	-0.08	0.85
7	$\text{HCOO}^{**} + \text{H}^* \leftrightarrow \text{H}_2 + \text{CO}_2^* + 2*$	-0.84	0.99	-0.34	1.11	-0.15	1.30
8	$\text{COOH}^* + * \leftrightarrow \text{CO}_2^* + \text{H}^*$	-0.54	0.54	-0.48	0.68	-0.46	0.74
9	$\text{COOH}^* \leftrightarrow \text{COOHcis}^*$	0.05	0.45	0.00	0.52	-0.01	0.44
10	$\text{COOHcis}^* + * \leftrightarrow \text{CO}^* + \text{OH}^*$	1.30	1.33	0.55	0.70	0.51	1.00
11	$\text{COOHcis}^* + \text{H}^* \leftrightarrow \text{CO}^* + \text{H}_2\text{O}^*$	-0.33	0.55	-0.36	0.68	-0.30	0.87
12	$\text{HCO}^* + * \leftrightarrow \text{CO}^* + \text{H}^*$	0.07	0.59	-0.29	0.24	-0.26	0.28
13	$\text{OH}^* + \text{H}^* \leftrightarrow \text{H}_2\text{O}^* + *$	-1.64	0.26	-0.92	0.38	-0.81	0.61
14	$2\text{H}^* \leftrightarrow \text{H}_2 + 2*$	-0.49	0.57	-0.17	0.47	-0.07	0.49
15	$\text{CO}_2^* \leftrightarrow \text{CO}_2 + *$	0.02		0.02		0.05	
16	$\text{H}_2\text{O}^* \leftrightarrow \text{H}_2\text{O} + *$	0.10		0.14		0.20	
17	$\text{CO}^* \leftrightarrow \text{CO} + *$	0.21		0.62		0.67	

All the values are relative to infinite separation in initial/final states. All adsorption and desorption steps are found to be nonactivated and are assumed to be quasiequilibrated.

bidentate configuration (Figure 3) with its O ends on top of two nearest neighbor metal atoms. This structural data is in agreement with the available experimental (NEXAFS and IR)⁹¹ and theoretical evidence. It has a BE of -1.69 eV (-1.82 eV⁸³), -2.02 eV (-2.10 eV⁸⁴), and -2.19 eV on Au(111), Au(100), and Au(211), respectively.

The BEs of atomic hydrogen on Au(111), Au(100), and Au(211) are -1.90 eV (-2.03 eV,⁸³ -2.20 eV^{97,98}), -2.06 eV (-2.29 eV⁸⁴), and -2.11 eV (-2.32 eV⁹⁹), respectively. H* binds preferentially on the bridge sites on Au(100) and Au(211), and on the threefold sites on Au(111). The most stable binding configuration on Au(111) is at the fcc sites, although the hexagonal close packed (hcp) sites are found to be energetically quasidegenerate to the fcc sites.

Atomic oxygen prefers the threefold fcc site on Au(111), the fourfold hollow site on Au(100), and the twofold bridge site on the step edge of Au(211), with BEs of -2.41 eV (-2.43 eV¹⁰⁰), -2.69 eV (-2.85 eV¹⁰¹), and -2.80 eV (-2.83 eV¹⁰²), respectively. Hydroxyl prefers to adsorb in a top-tilted configuration on the bridge sites of all three Au facets with BEs of -1.36 eV (-1.47 eV¹⁰⁰), -1.96 eV, and -2.07 eV on Au(111), Au(100), and Au(211), respectively.

Carboxyl exhibits two stable adsorption configurations: (a) one with H pointing downward toward the surface, the trans isomer (COOH*) and (b) one with H pointing away from the surface, the cis isomer (COOHcis*). COOH* has a BE of -1.27 eV, -1.48 eV (-1.61 eV⁸⁴), and -1.58 eV on Au(111), Au(100), and Au(211), respectively. The formyl radical binds preferentially through its C atom to the top sites of all three Au facets, with BEs of -1.05 eV, -1.26 eV, and -1.38 eV on Au(111), Au(100), and Au(211), respectively.

Carbon monoxide (CO) binds through the carbon atom, with the C—O bond perpendicular to the surface. It binds preferentially to the top site on Au(111), and the twofold bridge sites on Au(100) and the step-edge of Au(211), with BEs of -0.21 eV (-0.26 eV⁸³), -0.62 eV (-0.62 eV⁸⁴), and -0.67 eV (-0.65 eV¹⁰³), respectively. Water binds weakly through its oxygen atom to the top site of the three Au facets with the plane containing all the atoms parallel to

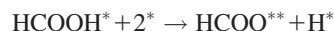
the surface. It has a BE of -0.10 eV (-0.11 eV,⁸³ -0.15 eV,¹⁰⁴ -0.12 eV⁹⁸), -0.14 eV, and -0.20 eV (-0.19 eV⁹⁹) on Au(111), Au(100), and Au(211), respectively.

Carbon dioxide (CO₂) binds weakly on all three Au facets, with BEs of -0.02 ~ -0.05 eV. CO₂ retains its gas-phase linear geometry and exhibits very weak site preference with several degenerate binding configurations.

Reaction barriers of elementary steps

The calculated E_A and reaction energies (ΔE) for all elementary steps studied are reported in Table 2. All activation energy barriers and reaction energies reported in the following text are relative to the reactant and product states at infinite separation.

HCOOH Activation. Here, we discuss three different pathways of HCOOH activation, namely, the HCOO, the COOH, and the HCO mediated pathways (Figure 7)



HCOOH* decomposition to HCOO** is found to proceed directly from the most stable, albeit weakly bound perpendicular configuration. The most favorable pathway involves

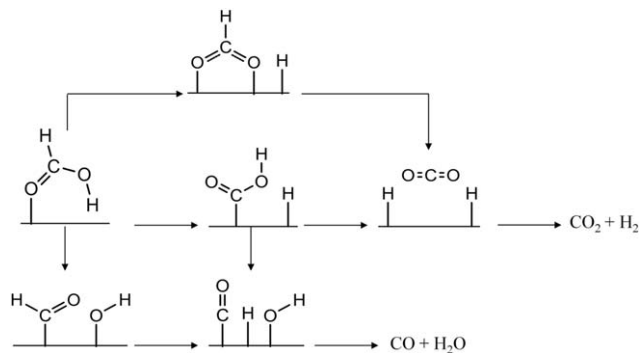


Figure 7. The three HCOOH decomposition pathways considered.

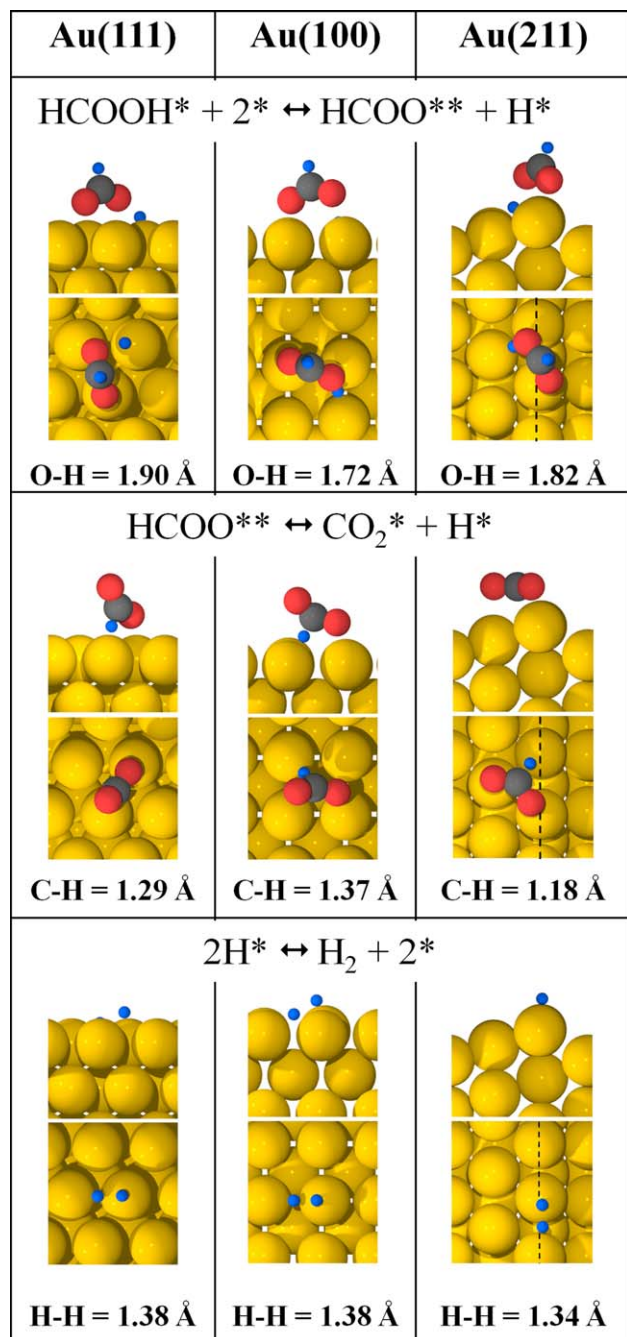


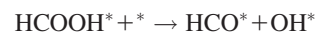
Figure 8. Side and top views of the transition states (TS) for the three kinetically relevant steps (as predicted by our microkinetic modeling results) on Au(111), Au(100), and Au(211) surfaces.

The lengths of the bond being broken/formed are reported for each transition state. Dotted black lines in the top views of Au(211) surface indicate the step-edge. [Color figure can be viewed in the online issue, which is available at wileyonlinelibrary.com.]

H abstraction from HCOOH* over the top site on Au(111), but bridge site on Au(100) and Au(211) surface. This step has a ΔE of 0.86 (0.89 eV⁸³), 0.42, and 0.26 eV, with E_A of 1.29 (1.36 eV⁸³), 0.87, and 0.98 eV on Au(111), Au(100), and Au(211), respectively

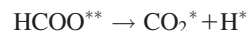


C—H bond scission in HCOOH*, yielding adsorbed COOH* and atomic hydrogen, is a two-step process. The first step is the rotation of HCOOH* to yield a metastable HCOOHpa* state. This rotation is quasi structure-insensitive, with a barrier of 0.55–0.63 eV on the three Au facets. HCOOHpa* is higher in energy than the most stable adsorbed state (HCOOH*), but it brings the carbonic hydrogen in FA closer to the three Au surfaces, thereby facilitating the C—H bond scission. The specific bond scission in HCOOHpa* to yield COOH* is an endothermic step, with E_A of 1.22, 0.83, and 0.87 eV on Au(111), Au(100), and Au(211), respectively

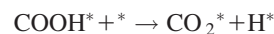


The dehydroxylation of HCOOH* to yield HCO* and OH* has a barrier of 2.16, 1.91, and 1.74 eV on Au(111), Au(100), and Au(211), respectively, significantly higher than the HCOO** and COOH* formation steps.

Product Formation.



H abstraction from HCOO** starts with the rotation of the HCOO** molecule such that the C—H bond becomes parallel to the Au surface, and one Au—O bond is broken just before the C—H bond scission over the top sites of all three Au facets (top site at the step edge for Au(211) facet). The H—C bond length in the transition state is 1.29, 1.37, and 1.18 Å on Au(111), Au(100), and Au(211), respectively (Figure 8), as compared to the bond length of 1.11 Å in adsorbed HCOO**. This step is slightly exothermic on Au(111) ($\Delta E = -0.35$ eV) and Au(100) ($\Delta E = -0.17$ eV) and near-thermo neutral on Au(211) ($\Delta E = -0.08$ eV). E_A for this step is relatively invariant of the model surface, with values of 0.80 (0.65 eV¹⁰⁵), 0.84, and 0.85 eV on Au(111), Au(100), and Au(211), respectively



Carboxyl decomposition to CO₂ is found to proceed directly from the more stable trans configuration (COOH*). The reaction on all three facets starts with rotation of carboxyl within its molecular plane, such that O—H bond scission takes place over the top site. Atomic hydrogen subsequently diffuses to the closest preferable site, and CO₂ settles in its physisorbed state. This step is exothermic, with ΔE of -0.54 (-0.49 eV⁹⁸), -0.48, and -0.46 eV, and has E_A of 0.54 (0.58 eV⁹⁸), 0.68 eV, and 0.74 eV on Au(111), Au(100), and Au(211), respectively



Contrary to the previous step, CO formation from carboxyl starts from the cis configuration of carboxyl. For this to take place, the most stable trans configuration of COOH* undergoes activated rotation (with E_A of 0.45, 0.52 and 0.44 eV on Au(111), Au(100), and Au(211), respectively), to yield the cis configuration (COOHcis*). The dissociation of COOHcis* takes place over the top site on all three Au facets, with E_A of 1.33 (1.25 eV⁹⁸), 0.70, and 1.00 eV on Au(111), Au(100), and Au(211), respectively

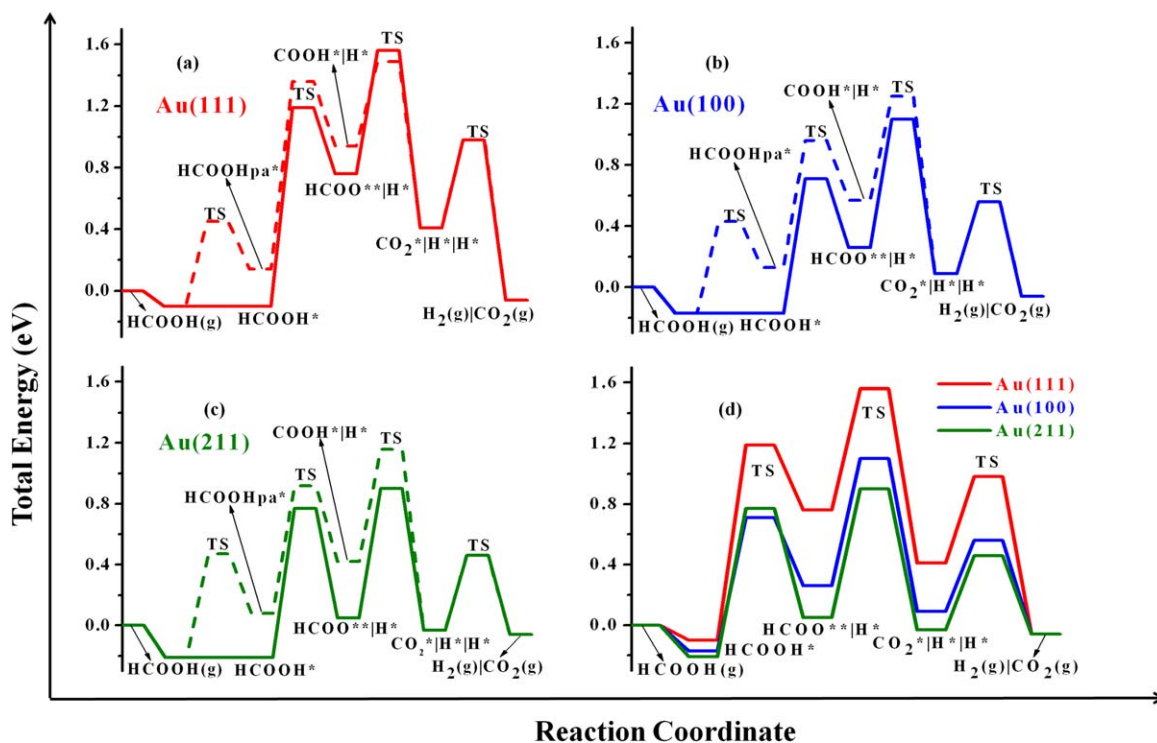
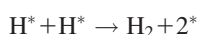


Figure 9. The two-dimensional PESs of FA decomposition reaction via the HCOO (solid lines) and COOH (dashed lines) mediated pathways on Au(111) (red) (a), Au(100) (blue) (b), and Au(211) (green) (c), and a comparison of the most favorable pathways (HCOO mediated) on all three facets (d).

Energy zero corresponds to the energy of HCOOH in the gas phase, away from the slab. A “|” between two adsorbates denotes that they are at infinite separation from each other. [Color figure can be viewed in the online issue, which is available at wileyonlinelibrary.com.]



H₂ recombinative desorption starts with two H* adsorbed on adjacent bridge sites, and the H—H bond formation takes place over the top site, for all three Au facets. The H—H bond length at the transition state are 1.38, 1.38, and 1.34 Å on Au(111), Au(100), and Au(211), respectively, (Figure 8) as compared to an H₂ gas-phase bond length of 0.75 Å.

Potential energy surfaces

The thermochemistry and activation energy barriers of various elementary steps described in the previous sections can be summarized in the form of two-dimensional potential energy surfaces (PESs) for the three Au facets, as shown in Figure 9. The PESs shown in Figure 9a–c compare the HCOO** and COOH* mediated pathways on the three Au facets respectively. On the basis of the DFT-derived energetics alone, the HCOO** mediated route appears to be the minimum energy path for FA decomposition on Au(100) and Au(211), whereas both HCOO** and COOH* mediated routes appear to be competitive for the Au(111) facet. Figure 9d compares the HCOO** pathway on all three Au facets, and one can suggest from here that Au(100) and Au(211) are expected to be significantly more active than the Au(111) facet.

Microkinetic modeling

A microkinetic model was developed using the results from these DFT calculations as initial guesses for the model parameters. With no adjustments to the DFT derived parameters, the microkinetic model predicts FA decomposition rates

that are 11 and 5 orders of magnitude lower on the Au(111) and Au(100)/Au(211) surfaces, respectively, than the measured experimental rates on Au/SiC. The reaction is predicted to take place via the HCOO mediated route, that is, $\text{HCOOH}(\text{g}) \rightarrow \text{HCOOH}^* \rightarrow \text{HCOO}^{**} + \text{H}^* \rightarrow \text{CO}_2^* + 2\text{H}^* \rightarrow \text{CO}_2(\text{g}) + \text{H}_2(\text{g})$, on all three facets, with 100% selectivity toward the dehydrogenation products; the rate of CO production is predicted to be negligible. We next carried out studies in which the kinetic parameters were adjusted from the initial values on these three Au facets in attempts to describe the results from reaction kinetic measurements (Table 3). The adjustable parameters that are modified during this process are the BEs of all surface species and transition state energies of all activated elementary steps. While this procedure gives a total of 26 parameters for our complex reaction network, sensitivity analysis showed that only the BEs of HCOO**, H*, and the transition state energies of the HCOO** formation and direct decomposition steps (Steps (3) and (6) in Table 2) were sensitive parameters. We then made systematic adjustments in these parameters until reasonable agreement between the experimentally measured and model predicted reaction rates was reached, and we subsequently used a gradient-based optimization algorithm in Matlab to obtain optimized values and confidence intervals for our adjustable parameters. The model predicted reaction orders and apparent activation energy barriers corresponding to the best-fitted solution are reported in Table 4, and are in close agreement with their experimental counterparts. In addition, the experimentally observed apparent activation energy barrier (59.6 kJ mol^{−1}) in the zero-order kinetic regime is in good agreement with past experimental studies

Table 3. Reaction Rates and Selectivities Obtained from the Kinetics Experiments on Au/SiC

	Temperature (K)	y(HCOOH)	y(He)	y(H ₂)	y(CO ₂)	Experimental Rates (μmol gcat ⁻¹ min ⁻¹)	Experimental Selectivity (CO ₂ /(CO ₂ +CO))
1	373	0.01	0.99	0.00	0.00	9.30	1.00
2	373	0.02	0.98	0.00	0.00	15.42	1.00
3	373	0.02	0.98	0.00	0.00	18.65	1.00
4	373	0.04	0.96	0.00	0.00	33.00	1.00
5	343	0.03	0.97	0.00	0.00	5.05	1.00
6	353	0.03	0.97	0.00	0.00	8.00	1.00
7	363	0.03	0.97	0.00	0.00	15.72	1.00
8	368	0.03	0.97	0.00	0.00	21.35	1.00
9	373	0.03	0.97	0.00	0.00	24.11	1.00
10	378	0.03	0.97	0.00	0.00	32.55	1.00
11	383	0.03	0.97	0.00	0.00	41.30	1.00
12	373	0.03	0.96	0.01	0.00	23.91	1.00
13	373	0.03	0.94	0.04	0.00	24.09	1.00
14	373	0.03	0.92	0.06	0.00	24.32	1.00
15	373	0.03	0.96	0.00	0.01	23.69	1.00
16	373	0.03	0.95	0.00	0.03	23.76	1.00
17	373	0.03	0.92	0.00	0.06	23.97	1.00

y denotes mole fraction in the inlet feed. The catalyst sample used in these studies was reduced *in situ*, prior to the reaction, at 623 K under pure hydrogen flow (30 cm³ (STP) min⁻¹) for 4 h. All the reaction rates reported here correspond to the steady-state values. The reaction was allowed to run for at least an hour after changing the conditions and before taking any measurements, and the steady state was confirmed by taking several readings over the next hour; hence, each data point is an average of several experimental runs.

on numerous supported Au catalysts.^{61,62,106} Figure 10 shows the PES for the best-fitted solution, compared with the DFT derived PESs for the three Au facets. Here, we only report the energetics of the closed catalytic cycle that is found to carry the entire reaction flux; the energetics of other elementary steps, which do not carry much flux from reactants to products are not included in the figure. We can see from this figure that the adjustments needed in the DFT derived initial guesses to obtain good fits are too large to be attributed to the computational errors in our calculations, which are typically on the order of 0.1–0.2 eV. With > 0.95 ML of the surface predicted to be vacant under all conditions, we can also rule out any potential stabilization that might result from lateral adsorbate–adsorbate interactions.¹⁰⁷ In particular, an additional stabilization of the transition states for the HCOO** formation and decomposition steps by > 0.5 eV is required to obtain good fits with the experimental data, strongly suggesting that (1) the Au(111), Au(100), and Au(211) may not be the most accurate representation of the active sites for this reaction and (2) the active site might be an even more under-coordinated environment that would stabilize the transition states to a much greater extent than these three facets. This conclusion is a quantitative confirmation of a previous proposal put forward by Iglesia and Ojeda based on their experimental reactivity studies for the same reaction.⁶¹ Importantly, similar suggestions for the reactivity of single metal atoms or very small metal nanoclusters have been made in the literature for other reactions as well.^{108–111}

Rate Determining Step. The individual reaction fluxes of the elementary steps reveal that the overall reaction proceeds entirely through the “direct HCOO**” route, and no reaction flux is observed through any of the COOH* mediated pathways. We further analyzed the reaction mechanism and the rate determining steps in the reaction scheme using Campbell’s degree of rate control,^{112–114} which quantifies the kinetic importance of an elementary step in a reaction scheme by computing the relative change in the overall reaction rate upon changing the forward and reverse rate constants for that

step, while holding the equilibrium constant for that step as well as the rate constants for all other steps constant. In this formalism, the degree of rate control (X_{RC}) of each elementary step can be evaluated using the following relation

$$X_{RC,i} = \frac{k_i}{r} \left(\frac{\partial r}{\partial k_i} \right)_{K_{i,eq}, k_j}$$

where k_i is the rate constant for step i , $K_{i,eq}$ is the equilibrium constant for this step, and r is the overall reaction rate. For all equilibrated steps (including the adsorption/desorption steps that were assumed to be quasiequilibrated), $X_{RC,i}$ is 0. Table 5 gives the $X_{RC,i}$ for the kinetically relevant steps in our reaction mechanism. For the “best-fitted solution,” Step 6 exhibits the highest degree of rate control for all reaction conditions and, hence, is the most rate controlling.

Active sites

The results from our microkinetic model suggest that Au(111), Au(100), and Au(211) are, in all likelihood, not the best representation of active sites for this reaction on SiC-supported Au catalysts. Thus, the major contributors to the overall rates could potentially be the Au atoms with lower (< 7) Au–Au coordination that exhibit even greater stabilization of reaction intermediates and transition states than the more open facets studied here [(100) and (211)]. To gain further insights into the nature of the active sites, we synthesized different catalyst samples with a varying degree of Au dispersion by treating the initial catalyst in flowing H₂ at different temperatures (623, 673, 723, 973, and 1073 K) for 8 h, prior to using these materials as catalysts for reaction

Table 4. Experimental and Model Predicted Reaction Orders and Apparent Activation Energy Barriers

	Experiment	Model
HCOOH	0.95 ± 0.06	0.99
CO ₂	0.01 ± 0.003	0.00
H ₂	0.01 ± 0.003	0.00
E _A	59.6 ± 1.6 kJ mol ⁻¹	60.2 kJ mol ⁻¹

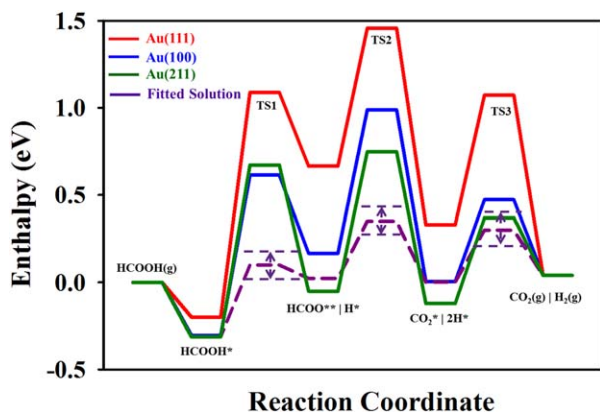


Figure 10. Enthalpy surfaces for FA decomposition via the HCOO** mediated pathway on Au(111), Au(100), and Au(211) facets (red, blue, green, respectively) as obtained directly from DFT calculations, and that corresponding to the best fitted solution (violet) along with the confidence intervals for the transition states.

TS denotes the transition state for the respective elementary step. This sequence of elementary steps carries almost the entire flux from reactants to products for all experimental conditions studied. [Color figure can be viewed in the online issue, which is available at wileyonlinelibrary.com.]

kinetic studies. Typically, the catalysts that are prereduced at low temperatures are more highly dispersed (and less sintered) than the materials that are prereduced at high temperatures.

Particle-Size Distribution. Figure 11 shows representative STEM images of the five catalysts that were used to determine the Au particle-size distribution (Figure 12) in these samples. This technique allows for imaging Au nanoparticles as low as 0.3 nm in size. It was observed that reducing the catalysts under a H₂ stream at increasingly elevated temperatures resulted in increased averaged Au particle sizes, as reported in Table 6.

Kinetic Reaction Rate Measurements. Reaction kinetic measurements were performed to obtain the FA decomposition rates on five catalysts under same operating conditions ($T = 413$ K, Total inlet flow rate = 100 mL min⁻¹, Inlet feed composition = 2.5% FA and 97.5% He). A monotonic decrease in the reaction rates with an increase in the prereduction temperature (and the average particle size) was observed, as shown in Table 6.

Additionally, it is observed that the number (and relative abundance) of subnanometer sized Au clusters decreases sharply upon increasing the calcination temperature. As a result, these reactivity trends provide a first indication that the number of subnanometer sized Au clusters in the catalyst may be correlated with the overall reaction rate. This hypothesis is consistent with past experimental studies^{60,61,106} that have postulated that this remarkable activity on supported Au catalysts arises from subnanometric Au clusters that are undetected in TEM micrographs. To quantify the contributions of different Au atoms in the catalytic particles/clusters to the overall reaction rate, we first classify the different kinds of Au atoms that are present in any

given cluster into four categories: (1) Corner (C) atoms: CN = 1–4, (2) Perimeter (P) atoms: CN = 5 and 6, (3) Terrace (T) atoms: CN = 7–9, and (4) Bulk (B) atoms: CN ≥ 9, where CN refers to the Au–Au coordination number. Surface (S) atoms are defined as the sum total of the C, P, and T atoms.

In their work on the WGS reaction on supported Au catalysts, Ribeiro and coworkers^{115–117} used physical models of Au clusters as truncated cuboctahedra to develop relations for determining the variation of the C, P, and T sites with the number averaged Au particle size. However, these relations hold true only for particles with diameter (d) > 1.6 nm. Therefore, and given our STEM data, we attempted to develop physical models of Au clusters with $d < 1.6$ nm to obtain the corresponding relations that provide the dependence of the C, P, and T sites on the average Au particle size. For that purpose, we used the results of past computational studies which used DFT to identify the most stable configurations of Au_{*n*} clusters (with $2 < n < 20$) in the gas phase,^{118–121} along with our physical models. The relative abundance of the C, P, and T sites is highly dependent on the choice of the cluster shape for $d < 1.6$ nm. As there is no general agreement in the literature on the most stable structures for these small clusters, a computational methodology must be adopted to this end. This approach would involve modeling a SiC support, performing *ab initio* molecular dynamics^{122–124} simulations to determine the most stable configurations of different sized Au clusters on this support under reaction conditions, and finally counting the number of C, P, and T sites in these configurations to develop the structure-site density relations for quantifying the contributions from each of these sites toward the overall rates. This approach is an ongoing endeavor and will be presented in a future report. However, as a first approximation, we treat these sites together as the total number/fraction of surface (S) atoms (i.e., C + P + T) is invariant of the actual distribution. In particular, all atoms in clusters of $d < 1.6$ nm can be assumed to be surface atoms (100% dispersion) without loss of accuracy.

The total moles of surface Au in the catalysts can then be calculated using the following relation

$$\text{Total moles of surface Au} = \left(\frac{\sum_n f(d) t(d)}{\sum_n t(d)} \right) \times \text{Total moles of Au in the catalyst}$$

where, $f(d)$ is the fraction of surface atoms in the cluster of diameter d (Table 7), $t(d)$ is the total number of atoms in that cluster, and the summation is performed over all the Au clusters that were identified from the STEM image of that catalyst, that is, the full particle-size distribution was used for each sample. The TOFs normalized to the surface Au moles and total Au moles are plotted against the average particle size in Figure 13, and these plots can be used to draw the following key conclusions:

Table 5. Campbell's Degree of Rate Control for Kinetically Relevant Steps

Step #	Elementary Step	X_{RC}
3	$\text{HCOOH}^* + 2^* \leftrightarrow \text{HCOO}^{**} + \text{H}^*$	0.25
6	$\text{HCOO}^{**} \leftrightarrow \text{CO}_2^* + \text{H}^*$	0.64
14	$2\text{H}^* \leftrightarrow \text{H}_2 + 2^*$	0.10

These numbers are reported for the reaction condition # 9 of Table 3.

Table 6. Average Particle Size (as Determined by STEM) and Experimentally Measured Reaction Rates on the Five Different Au/SiC Catalysts

Catalyst Sample #	Prereduction Temperature (K)	Number of Total/ Subnanometer sized Au Clusters Analyzed	Number Average Particle Size (d [nm])	Experimentally Observed Reaction Rate ($\mu\text{mol gcat}^{-1} \text{min}^{-1}$)
1	623	6860/1248	2.55	178.58
2	673	4837/636	3.09	129.93
3	723	3887/213	3.23	97.84
4	973	1119/0	7.53	9.02
5	1073	1153/0	10.74	2.64

1. A decreasing trend in the rate per surface site with average Au particle size (Figure 13a) indicates the heterogeneity of the surface Au sites, that is, all surface sites do not contribute equally to the overall reaction rate.
2. Figure 13b shows that the rate per total mole of Au catalysts varies as $d^{-2.95}$, whereas Table 7 suggests that the fraction of terrace, perimeter, and corner sites vary as $d^{-0.7}$, $d^{-1.8}$, and $d^{-2.9}$, respectively. Thus, the variation in FA decomposition rate per total mole of Au seems to correlate with the “corner model,” that is, the rate per corner site is independent of the Au particle size, thereby implying that corner sites might be the dominant active sites for this reaction. As mentioned earlier, this conclusion is based on the assumption that

the $d^{-2.9}$ dependence of the corner sites will be valid over the entire particle size range, and further studies to confirm this for smaller clusters ($d < 1.6$ nm) will be needed.

Conclusions

Periodic, self-consistent DFT calculations were performed to determine the energetics of 13 adsorbed intermediates for FA decomposition, as well as the activation energy barriers and pre-exponential factors of 13 activated elementary steps on Au(111), Au(100), and Au(211) surfaces, which were chosen as the representative stable model facets of Au nanoparticles on SiC support. The DFT results suggest that the surface species and transition states are stabilized as the Au–

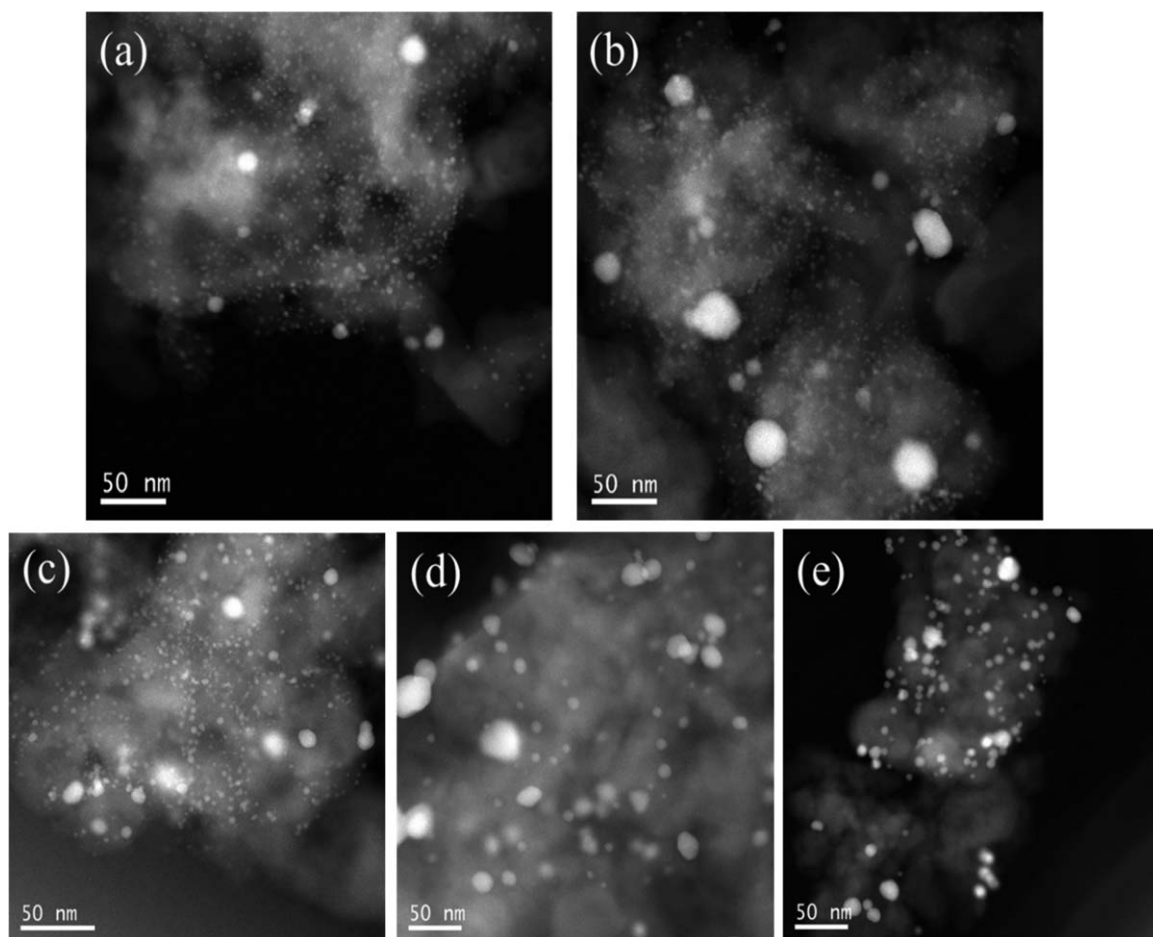


Figure 11. Typical STEM images of Au/SiC catalysts used to determine the Au particle-size distributions.
The prereduction temperatures for these catalysts are (a) 623 K, (b) 673 K, (c) 723 K, (d) 973 K, and (e) 1073 K.

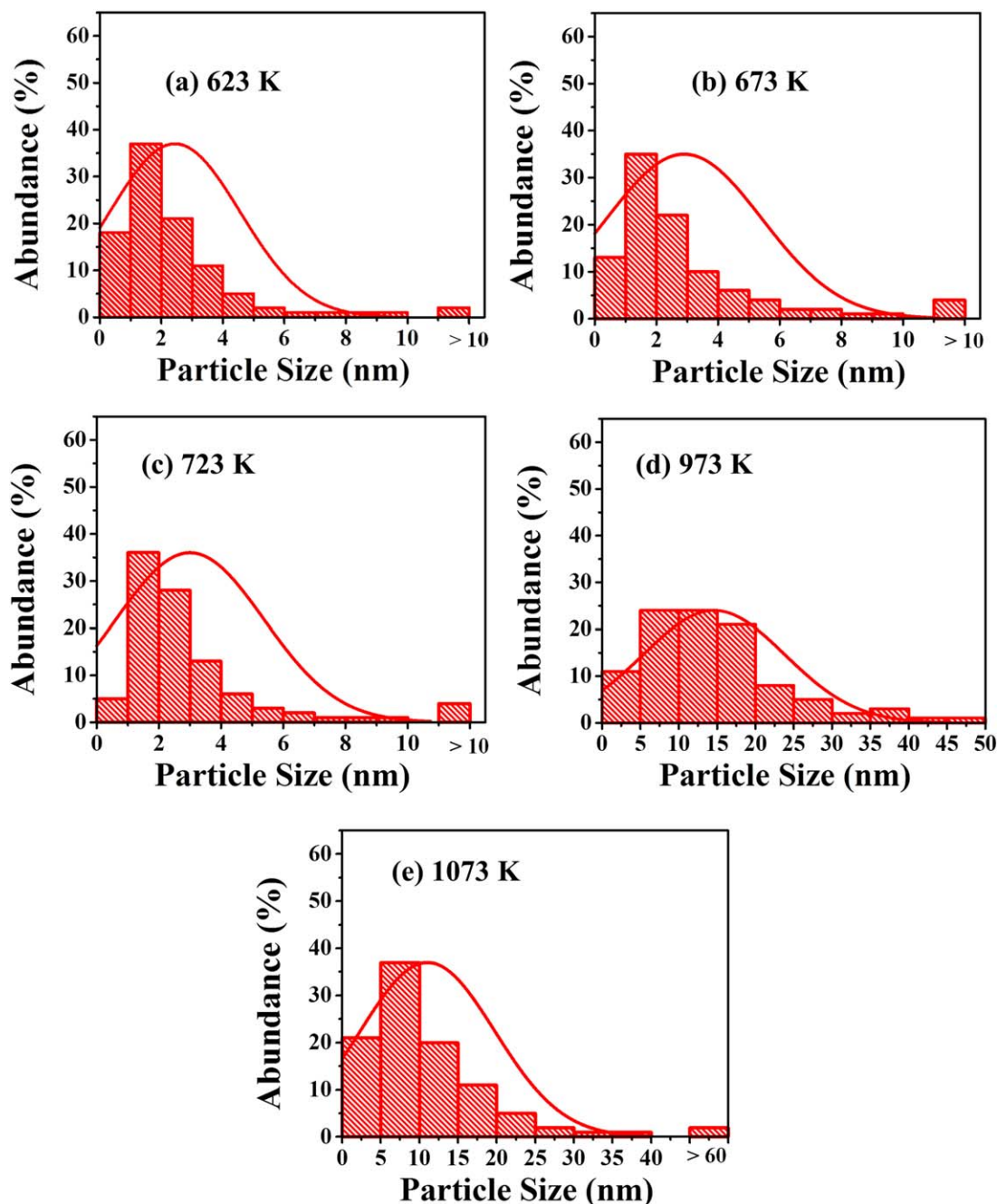


Figure 12. Histograms depicting the Au particle-/cluster-size distributions for the Au/SiC catalysts prereduced at 623–1073 K for 8 h.

[Color figure can be viewed in the online issue, which is available at wileyonlinelibrary.com.]

Au coordination of surface atoms decreases, and the reaction rates follow the order: Au(211) \approx Au(100) > Au(111).

A mean-field microkinetic model was used to describe the experimental rate and selectivity data that were collected

under realistic conditions on Au/SiC. Our “best fitted solution” from the microkinetic model shows a good description of the experimental data ($R^2 = 0.98$), and good agreement between the model predicted apparent activation energy barriers and

Table 7. Relations Used to Determine the Fraction of Different Sites from the Number-Average Particle Size Obtained From the STEM Images

Type of Surface Site \rightarrow				
Particle Size \downarrow	Terrace (T)	Perimeter (P)	Corner (C)	Surface (S)
< 1.6 nm	#	#	#	1.0
≥ 1.6 nm ¹¹⁵	$0.90 d^{-0.7}$	$0.46 d^{-1.8}$	$0.54 d^{-2.9}$	$0.90 d^{-0.7} + 0.46 d^{-1.8} + 0.54 d^{-2.9}$

The actual relations for C, P, and T sites for $d < 1.6$ nm are currently unavailable. All the relations presented here give the ratio of that particular site to the total Au atoms in the catalyst. For instance, for $d > 1.6$ nm, (Number of terrace atoms/Total Au atoms) = $0.90 d^{-0.7}$ and so forth.

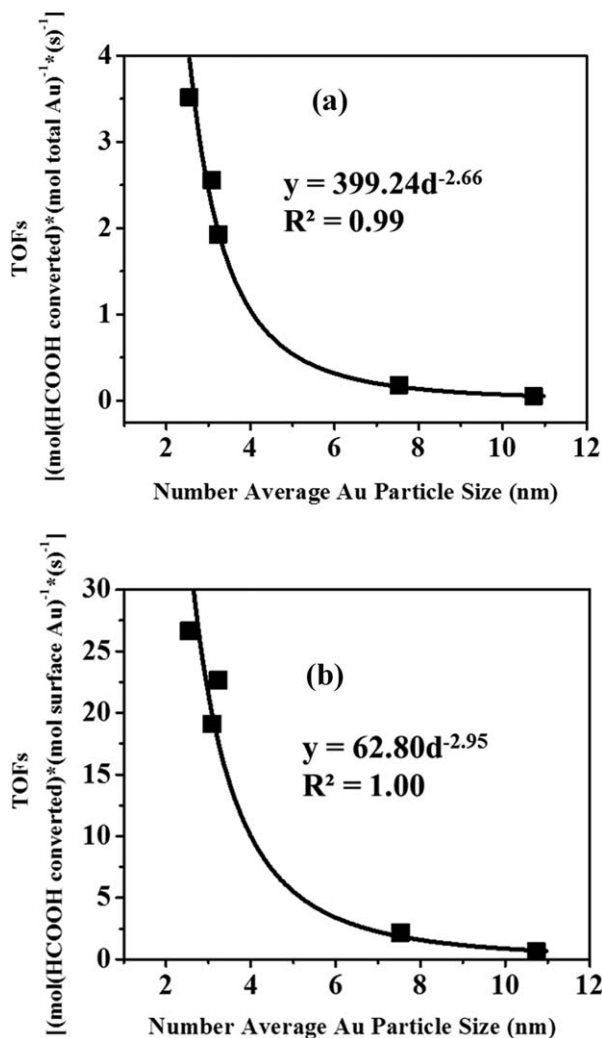


Figure 13. FA decomposition rate normalized by (a) surface Au moles and (b) total Au moles (2% FA inlet feed at 413 K, 1 atm) on Au/SiC catalysts.

reaction orders with their experimental counterparts. The reaction is predicted to proceed via the formate mediated route. Importantly, the closed catalytic cycle that adequately describes the FA decomposition mechanism on Au catalysts is found to be comprised of three elementary steps: $\text{HCOOH}^* \rightarrow \text{HCOO}^{**} + \text{H}^*$, $\text{HCOO}^{**} \rightarrow \text{CO}_2^* + \text{H}^*$, and $2\text{H}^* \rightarrow \text{H}_2(\text{g})$.

A comparison of the DFT derived BEs and E_{AS} with the parameters obtained upon fitting the microkinetic model to the experimental data suggests that Au(111), Au(100), and Au(211) might not provide the most accurate representation of the active site on supported Au catalysts. Further reaction rate experiments and measurements of the Au particle-size distribution using STEM corroborated this claim that the coordinatively unsaturated corner sites, with Au–Au coordination of ≤ 4 , are most likely the dominant active sites for this reaction. Further DFT studies on Au clusters that possess atoms with Au–Au coordination number ≤ 4 will be needed to identify the exact nature of active site for FA decomposition on supported Au nanoparticles. We are currently exploring synthetic protocols suggested in the literature^{52,59,60,125–128} for synthesizing catalysts with atomically dispersed gold to further advance our tentative conclusion regarding the

importance of highly under-coordinated Au sites in this chemistry.

Acknowledgments

This contribution is dedicated to the 90th birthday celebration of R. B. Bird. His legacy of excellence and scientific rigor has inspired generations of Chemical Engineers, including J.A.D. and M.M. The material presented here is based upon work supported as part of the Institute of Atom-efficient Chemical Transformation (IACT), an Energy Frontier Research Center funded by the U.S. Department of Energy, Office of Science, and Office of Basic Energy Sciences. The computational work was performed in part using supercomputing resources from the following institutions: EMSL, a national scientific user facility at Pacific Northwestern National Laboratory (PNNL); the Center for Nanoscale Materials (CNM) at Argonne National Laboratory (ANL); and the National Energy Research Scientific Computing Center (NERSC). EMSL is sponsored by the Department of Energy's Office of Biological and Environmental Research located at PNNL. CNM and NERSC are supported by the U.S. Department of Energy, Office of Science, under contracts DEAC02-06CH11357 and DE-AC02-05CH11231, respectively.

Literature Cited

- Alonso DM, Bond JQ, Dumesic JA. Catalytic conversion of biomass to biofuels. *Green Chem.* 2010;12:1493–1513.
- Tilman D, Socolow R, Foley JA, Hill J, Larson E, Lynd L, Pacala S, Reilly J, Searchinger T, Somerville C, Williams R. Beneficial biofuels—the food, energy, and environment trilemma. *Science.* 2009;325:270–271.
- Bozell JJ, Petersen GR. Technology development for the production of biobased products from biorefinery carbohydrates—the US Department of Energy's "Top 10" revisited. *Green Chem.* 2010;12:539–554.
- Boddien A, Loges B, Junge H, Gaertner F, Noyes JR, Beller M. Continuous hydrogen generation from formic acid: highly active and stable ruthenium catalysts. *Adv Synth Catal.* 2009;351:2517–2520.
- Fellay C, Yan N, Dyson PJ, Laurenczy G. Selective formic acid decomposition for high-pressure hydrogen generation: a mechanistic study. *Chem Eur J.* 2009;15:3752–3760.
- Fellay C, Dyson PJ, Laurenczy G. A viable hydrogen-storage system based on selective formic acid decomposition with a ruthenium catalyst. *Angew Chem Int Ed.* 2008;47:3966–3968.
- Gan W, Dyson PJ, Laurenczy G. Hydrogen storage and delivery: immobilization of a highly active homogeneous catalyst for the decomposition of formic acid to hydrogen and carbon dioxide. *React Kinet Catal Lett.* 2009;98:205–213.
- Fukuzumi S. Bioinspired energy conversion systems for hydrogen production and storage. *Eur J Inorg Chem.* 2008;2008:1351–1362.
- Boddien A, Gaertner F, Jackstell R, Junge H, Spannenberg A, Baumann W, Ludwig R, Beller M. Ortho-metalation of iron(0) tri-benzylphosphine complexes: homogeneous catalysts for the generation of hydrogen from formic acid. *Angew Chem Int Ed.* 2010;49:8993–8996.
- Johnson TC, Morris DJ, Wills M. Hydrogen generation from formic acid and alcohols using homogeneous catalysts. *Chem Soc Rev.* 2010;39:81–88.
- Rackemann DW, Doherty WOS. A review on the production of levulinic acid and furanics from sugars. *Proceedings of the 34th Conference of the Australian Society of Sugar Cane Technologists held at Cairns, Queensland, Australia, 2012:20-M 20.*
- Zhang T, Wyman CE. Integrated production of levulinic acid and furfural from cellulosic biomass. *Abstr Pap Am Chem Soc.* 2011;241.
- Girisuta B, Janssen LPBM, Heeres HJ. Kinetic study on the acid-catalyzed hydrolysis of cellulose to levulinic acid. *Ind Eng Chem Res.* 2007;46:1696–1708.

14. Bond JQ, Alonso DM, Wang D, West RM, Dumesic JA. Integrated catalytic conversion of gamma-valerolactone to liquid alkenes for transportation fuels. *Science*. 2010;327:1110–1114.
15. Braden DJ, Hena CA, Heltzel J, Maravelias CT, Dumesic JA. Production of liquid hydrocarbon fuels by catalytic conversion of biomass-derived levulinic acid. *Green Chem*. 2011;13:1755–1765.
16. Serrano-Ruiz JC, Braden DJ, West RM, Dumesic JA. Conversion of cellulose to hydrocarbon fuels by progressive removal of oxygen. *Appl Catal B*. 2010;100:184–189.
17. Columbia MR, Thiel PA. The interaction of formic-acid with transition-metal surfaces, studied in ultrahigh-vacuum. *J Electroanal Chem*. 1994;369:1–14.
18. Madix RJ. Surface-reaction modifiers—general overview. *Abstr Pap Am Chem Soc*. 1980;180:26—PHYS.
19. Larson LA, Dickinson JT. Decomposition of formic-acid on Ru(1010). *Surf Sci*. 1979;84:17–30.
20. Sun YK, Weinberg WH. Catalytic decomposition of formic-acid on Ru(001)—transient measurements. *J Chem Phys*. 1991;94:4587–4599.
21. Solymosi F, Kiss J, Kovacs I. Adsorption of hcooh on Rh(111) and its reaction with preadsorbed oxygen. *Surf Sci*. 1987;192:47–65.
22. Jorgensen SW, Madix RJ. Active oxygen on group viii metals—activation of formic-acid and formaldehyde on Pd(100). *J Am Chem Soc*. 1988;110:397–400.
23. Bulushev DA, Beloshapkin S, Ross JRH. Hydrogen from formic acid decomposition over Pd and Au catalysts. *Catal Today*. 2010;154:7–12.
24. Solymosi F, Koos A, Liliom N, Ugrai I. Production of CO-free H₂ from formic acid. A comparative study of the catalytic behavior of Pt metals on a carbon support. *J Catal*. 2011;279:213–219.
25. Ying DHS, Madix RJ. Thermal-desorption study of formic-acid decomposition on a clean Cu(110) surface. *J Catal*. 1980;61:48–56.
26. Boddien A, Mellmann D, Gaertner F, Jackstell R, Junge H, Dyson PJ, Laurenczy G, Ludwig R, Beller M. Efficient dehydrogenation of formic acid using an iron catalyst. *Science*. 2011;333:1733–1736.
27. Koos A, Solymosi F. Production of CO-free H-2 by formic acid decomposition over Mo₂C/carbon catalysts. *Catal Lett*. 2010;138:23–27.
28. Flaherty DW, Berglund SP, Mullins CB. Selective decomposition of formic acid on molybdenum carbide: a new reaction pathway. *J Catal*. 2010;269:33–43.
29. McCarty J, Madix RJ. Study of kinetics and mechanism of decomposition of formic-acid on carburized and graphitized Ni(110) using AES, LEED and flash desorption. *J Catal*. 1975;38:402–417.
30. Kubota J, Bandara A, Wada A, Domen K, Hirose C. IRAS study of formic acid decomposition on NiO(111)/Ni(111) surface: comparison of vacuum and catalytic conditions. *Surf Sci*. 1996;368:361–365.
31. Dilara PA, Vohs JM. TPD and HREELS investigation of the reaction of formic-acid on ZrO₂(100). *J Phys Chem*. 1993;97:12919–12923.
32. Larsson R, Jamroz MH, Borowiak MA. On the catalytic decomposition of formic acid. I. The activation energies for oxide catalysis. *J Mol Catal A Chem*. 1998;129:41–51.
33. Senanayake SD, Mullins DR. Redox pathways for HCOOH decomposition over CeO₂ surfaces. *J Phys Chem C*. 2008;112:9744–9752.
34. Peng XD, Barteau MA. Acid-base properties of model MgO surfaces. *Langmuir*. 1991;7:1426–1431.
35. Outka DA, Madix RJ. Acid-base and nucleophilic chemistry of atomic oxygen on the Au(110) surface—reactions with formic-acid and formaldehyde. *Surf Sci*. 1987;179:361–376.
36. Lin C-H, Chen C-L, Wang J-H. Mechanistic studies of water-gas-shift reaction on transition metals. *J Phys Chem C*. 2011;115:18582–18588.
37. Davis BH, Jacobs G, Patterson PM, Graham UM, Crawford AC. Low temperature water gas shift: the link between the catalysis of WGS and formic acid decomposition over Pt/Ceria. *Int J Hydrogen Energy*. 2005;30:1265–1276.
38. Gokhale AA, Dumesic JA, Mavrikakis M. On the mechanism of low-temperature water gas shift reaction on copper. *J Am Chem Soc*. 2008;130:1402–1414.
39. Liu C, Chen M, Du C, Zhang J, Yin G, Shi P, Sun Y. Durability of ordered mesoporous carbon supported Pt particles as catalysts for direct formic acid fuel cells. *Int J Electrochem Sci*. 2012;7:10592–10606.
40. Rice C, Ha S, Masel RI, Wieckowski A. Catalysts for direct formic acid fuel cells. *J Power Sources*. 2003;115:229–235.
41. Yu XW, Pickup PG. Codeposited PtSb/C catalysts for direct formic acid fuel cells. *J Power Sources*. 2011;196:7951–7956.
42. Yinghui P, Ruiming Z, Blair SL. Anode poisoning study in direct formic acid fuel cells. *Electrochem Solid-State Lett*. 2009;12:B23–B26.
43. Markovic NM, Ross PN. Surface science studies of model fuel cell electrocatalysts. *Surf Sci Rep*. 2002;45:121–229.
44. Xingwen Y, Pickup PG. Recent advances in direct formic acid fuel cells (DFAFC). *J Power Sources*. 2008;182:124–132.
45. Choi J-H, Jeong K-J, Dong Y, Han J, Lim T-H, Lee J-S, Sung Y-E. Electro-oxidation of methanol and formic acid on PtRu and PtAu for direct liquid fuel cells. *J Power Sources*. 2006;163:71–75.
46. Brandon NP, Skinner S, Steele BCH. Recent advances in materials for fuel cells. *Annu Rev Mater Res*. 2003;33:183–213.
47. Xu JB, Zhao TS, Liang ZX. Carbon supported platinum-gold alloy catalyst for direct formic acid fuel cells. *J Power Sources*. 2008;185:857–861.
48. Sheng Z, Yuyan S, Geping Y, Yuehe L. Facile synthesis of PtAu alloy nanoparticles with high activity for formic acid oxidation. *J Power Sources*. 2010;195:1103–1106.
49. Haruta M, Kobayashi T, Sano H, Yamada N. Novel gold catalysts for the oxidation of carbon-monoxide at a temperature far below 0-degrees-C. *Chem Lett*. 1987;405–408.
50. Hutchings GJ. Vapor-phase hydrochlorination of acetylene—correlation of catalytic activity of supported metal chloride catalysts. *J Catal*. 1985;96:292–295.
51. Sa J, Goguet A, Taylor SFR, Tiruvalam R, Kiely CJ, Nachttegaal M, Hutchings GJ, Hardacre C. Influence of methyl halide treatment on gold nanoparticles supported on activated carbon. *Angew Chem Int Ed*. 2011;50:8912–8916.
52. Guzman J, Gates BC. Gold nanoclusters supported on MgO: synthesis, characterization, and evidence of Au(6). *Nano Lett*. 2001;1:689–692.
53. Janssens TVW, Clausen BS, Hvolbaek B, Falsig H, Christensen CH, Bligaard T, Norskov JK. Insights into the reactivity of supported Au nanoparticles: combining theory and experiments. *Top Catal*. 2007;44:15–26.
54. Gong J. Structure and surface chemistry of gold-based model catalysts. *Chem Rev*. 2012;112:2987–3054.
55. Coquet R, Howard KL, Willock DJ. Theory and simulation in heterogeneous gold catalysis. *Chem Soc Rev*. 2008;37:2046–2076.
56. Davis RJ. All that glitters is not Au-0. *Science*. 2003;301:926–927.
57. Bond GC, Thompson DT. Catalysis by gold. *Catal Rev Sci Eng*. 1999;41:319–388.
58. Hashmi ASK, Hutchings GJ. Gold catalysis. *Angew Chem Int Ed*. 2006;45:7896–7936.
59. Guzman J, Anderson BG, Vinod CP, Ramesh K, Niemantsverdriet JW, Gates BC. Synthesis and reactivity of dimethyl gold complexes supported on MgO: characterization by infrared and x-ray absorption spectroscopies. *Langmuir*. 2005;21:3675–3683.
60. Yi N, Saltsburg H, Flytzani-Stephanopoulos M. Hydrogen production by dehydrogenation of formic acid on atomically dispersed gold on ceria. *ChemSuschem*. 2013;6:816–819.
61. Ojeda M, Iglesia E. Formic acid dehydrogenation on Au-based catalysts at near-ambient temperatures. *Angew Chem Int Ed*. 2009;48:4800–4803.
62. Gazsi A, Bansagi T, Solymosi F. Decomposition and reforming of formic acid on supported Au catalysts: production of CO-free H-2. *J Phys Chem C*. 2011;115:15459–15466.
63. Gokhale AA, Kandoi S, Greeley JP, Mavrikakis M, Dumesic JA. Molecular-level descriptions of surface chemistry in kinetic models using density functional theory. *Chem Eng Sci*. 2004;59:4679–4691.
64. Hammer B, Hansen LB, Norskov JK. Improved adsorption energetics within density-functional theory using revised Perdew-Burke-Ernzerhof functionals. *Phys Rev B*. 1999;59:7413–7421.
65. Greeley J, Norskov JK, Mavrikakis M. Electronic structure and catalysis on metal surfaces. *Annu Rev Phys Chem*. 2002;53:319–348.
66. Neugebauer J, Scheffler M. Adsorbate-substrate and adsorbate-adsorbate interactions of Na and K adlayers on Al(111). *Phys Rev B*. 1992;46:16067–16080.
67. Bengtsson L. Dipole correction for surface supercell calculations. *Phys Rev B*. 1999;59:12301–12304.
68. Chadi DJ, Cohen ML. Special points in brillouin zone. *Phys Rev B*. 1973;8:5747–5753.
69. Monkhorst HJ, Pack JD. Special points for brillouin-zone integrations. *Phys Rev B*. 1976;13:5188–5192.
70. Vanderbilt D. Soft self-consistent pseudopotentials in a generalized eigenvalue formalism. *Phys Rev B*. 1990;41:7892–7895.

71. Perdew JP, Chevary JA, Vosko SH, Jackson KA, Pederson MR, Singh DJ, Fiolhais C. Atoms, molecules, solids, and surfaces—applications of the generalized gradient approximation for exchange and correlation. *Phys Rev B*. 1992;46:6671–6687.
72. White JA, Bird DM. Implementation of gradient-corrected exchange-correlation potentials in Car-Parrinello total-energy calculations. *Phys Rev B*. 1994;50:4954–4957.
73. Kresse G, Furthmüller J. Efficiency of ab-initio total energy calculations for metals and semiconductors using a plane-wave basis set. *Comput Mater Sci*. 1996;6:15–50.
74. Donohue JL. *The Structures of the Elements*. New York: Wiley, 1974:222.
75. Henkelman G, Uberuaga BP, Jonsson H. A climbing image nudged elastic band method for finding saddle points and minimum energy paths. *J Chem Phys*. 2000;113:9901–9904.
76. Henkelman G, Jonsson H. Improved tangent estimate in the nudged elastic band method for finding minimum energy paths and saddle points. *J Chem Phys*. 2000;113:9978–9985.
77. Greeley J, Mavrikakis M. A first-principles study of surface and subsurface H on and in Ni(111): diffusional properties and coverage-dependent behavior. *Surf Sci*. 2003;540:215–229.
78. Grabow LC, Mavrikakis M. Mechanism of methanol synthesis on Cu through CO₂ and CO hydrogenation. *ACS Catal*. 2011;1:365–384.
79. Grabow LC, Gokhale AA, Evans ST, Dumesic JA, Mavrikakis M. Mechanism of the water gas shift reaction on Pt: first principles, experiments, and microkinetic modeling. *J Phys Chem C*. 2008;112:4608–4617.
80. Chakarova-Kack SD, Schroder E, Lundqvist BI, Langreth DC. Application of van der Waals density functional to an extended system: adsorption of benzene and naphthalene on graphite. *Phys Rev Lett*. 2006;96:14607-1–14607-4.
81. Sauer J, Ugliengo P, Garrone E, Saunders VR. Theoretical study of Van-der-waals complexes at surface sites in comparison with the experiment. *Chem Rev*. 1994;94:2095–2160.
82. Lopez N, Janssens TVW, Clausen BS, Xu Y, Mavrikakis M, Bligaard T, Norskov JK. On the origin of the catalytic activity of gold nanoparticles for low-temperature CO oxidation. *J Catal*. 2004;223:232–235.
83. Hu CQ, Ting SW, Chan KY, Huang W. Reaction pathways derived from DFT for understanding catalytic decomposition of formic acid into hydrogen on noble metals. *Int J Hydrogen Energy*. 2012;37:15956–15965.
84. Yu YL, Wang X, Lim KH. A DFT study on the adsorption of formic acid and its oxidized intermediates on (100) facets of Pt, Au, monolayer and decorated Pt@Au surfaces. *Catal Lett*. 2011;141:1872–1882.
85. Campbell CT, Daube KA. A surface science investigation of the water-gas shift reaction on Cu(111). *J Catal*. 1987;104:109–119.
86. Vanherwijnen T, Dejong WA. Kinetics and mechanism of the CO shift on Cu-ZnO.1. Kinetics of the forward and reverse CO shift reactions. *J Catal*. 1980;63:83–93.
87. Edwards JF, Schrader GL. Infrared-spectroscopy of Cu/ZnO catalysts for the water-gas shift reaction and methanol synthesis. *J Phys Chem*. 1984;88:5620–5624.
88. Bowker M, Hadden RA, Houghton H, Hyland JNK, Waugh KC. The mechanism of methanol synthesis on copper-zinc oxide alumina catalysts. *J Catal*. 1988;109:263–273.
89. Neophytides SG, Marchi AJ, Froment GF. Methanol synthesis by means of diffuse reflectance infrared fourier-transform and temperature-programmed reaction spectroscopy. *Appl Catal A*. 1992;86:45–64.
90. Sakakini B, Tabatabaei J, Watson MJ, Waugh KC, Zemicael FW. Identification of the intermediate involved in methanol synthesis by gaseous titration. *Faraday Discuss*. 1996;105:369–376.
91. Senanayake SD, Stacchiola D, Liu P, Mullins CB, Hrbek J, Rodriguez JA. Interaction of CO with OH on Au(111): HCOO, CO₃, and HOCO as key intermediates in the water-gas shift reaction. *J Phys Chem C*. 2009;113:19536–19544.
92. Meunier FC, Reid D, Goguet A, Shekhtman S, Hardacre C, Burch R, Deng W, Flytzani-Stephanopoulos M. Quantitative analysis of the reactivity of formate species seen by DRIFTS over a Au/Ce(La)O-2 water-gas shift catalyst: first unambiguous evidence of the minority role of formates as reaction intermediates. *J Catal*. 2007;247:277–287.
93. Nishimura K, Kunimatsu K, Machida K, Enyo M. Electrocatalysis of Pd + Au alloy electrodes.4. IR spectroscopic studies on the surface species derived from formaldehyde and formate in alkaline-solutions. *J Electroanal Chem*. 1989;260:181–192.
94. Chen Y, Cheng J, Hu P, Wang HF. Examining the redox and formate mechanisms for water-gas shift reaction on Au/CeO₂ using density functional theory. *Surf Sci*. 2008;602:2828–2834.
95. Duan S, Ji YF, Fang PP, Chen YX, Xu X, Luo Y, Tian ZQ. Density functional theory study on the adsorption and decomposition of the formic acid catalyzed by highly active mushroom-like Au@Pd/Pt trimetallic nanoparticles. *Phys Chem Chem Phys*. 2013;15:4625–4633.
96. Zhong WH, Liu YX, Zhang DJ. Theoretical study of methanol oxidation on the PtAu(111) bimetallic surface: CO pathway vs non-CO pathway. *J Phys Chem C*. 2012;116:2994–3000.
97. Greeley J, Mavrikakis M. Surface and subsurface hydrogen: adsorption properties on transition metals and near-surface alloys. *J Phys Chem B*. 2005;109:3460–3471.
98. Huang S-C, Lin C-H, Wang JH. Trends of water gas shift reaction on close-packed transition metal surfaces. *J Phys Chem C*. 2010;114:9826–9834.
99. Barton DG, Podkolzin SG. Kinetic study of a direct water synthesis over silica-supported gold nanoparticles. *J Phys Chem B*. 2005;109:2262–2274.
100. Ford DC, Nilekar AU, Xu Y, Mavrikakis M. Partial and complete reduction of O-2 by hydrogen on transition metal surfaces. *Surf Sci*. 2010;604:1565–1575.
101. Jalili S, Isfahani AZ, Habibpour R. Atomic oxygen adsorption on Au (100) and bimetallic Au/M (M = Pt and Cu) surfaces. *Comput Theor Chem*. 2012;989:18–26.
102. Xu Y, Mavrikakis M. Adsorption and dissociation of O-2 on gold surfaces: effect of steps and strain. *J Phys Chem B*. 2003;107:9298–9307.
103. Mehmood F, Kara A, Rahman TS, Henry CR. Comparative study of CO adsorption on flat, stepped, and kinked Au surfaces using density functional theory. *Phys Rev B*. 2009;79:075422-1–075422-6.
104. Ojifinni RA, Froemming NS, Gong J, Pan M, Kim TS, White JM, Henkelman G, Mullins CB. Water-enhanced low-temperature CO oxidation and isotope effects on atomic oxygen-covered Au(111). *J Am Chem Soc*. 2008;130:6801–6812.
105. Liu SP, Jin P, Zhang DH, Hao C, Yang XM. Reaction mechanism for methanol oxidation on Au(1 1 1): a density functional theory study. *Appl Surf Sci*. 2013;265:443–451.
106. Bi Q-Y, Du X-L, Liu Y-M, Cao Y, He H-Y, Fan K-N. Efficient subnanometric gold-catalyzed hydrogen generation via formic acid decomposition under ambient conditions. *J Am Chem Soc*. 2012;134:8926–8933.
107. Grabow LC, Hvolbaek B, Norskov JK. Understanding trends in catalytic activity: the effect of adsorbate-adsorbate interactions for CO oxidation over transition metals. *Top Catal*. 2010;53:298–310.
108. Flytzani-Stephanopoulos M, Gates BC. Atomically dispersed supported metal catalysts. *Annu Rev Chem Biomol Eng*. 2012;3:545–574.
109. Fu Q, Weber A, Flytzani-Stephanopoulos M. Nanostructured Au-CeO₂ catalysts for low-temperature water-gas shift. *Catal Lett*. 2001;77:87–95.
110. Deng WL, De Jesus J, Saltsburg H, Flytzani-Stephanopoulos M. Low-content gold-ceria catalysts for the water-gas shift and preferential CO oxidation reactions. *Appl Catal A*. 2005;291:126–135.
111. Gates BC. Supported gold catalysts: new properties offered by nanometer and sub-nanometer structures. *Chem Commun*. 2013;49:7876–7877.
112. Campbell CT. Finding the rate-determining step in a mechanism—comparing DeDonder relations with the “degree of rate control.” *J Catal*. 2001;204:520–524.
113. Campbell CT. Micro- and macro-kinetics: their relationship in heterogeneous catalysis. *Top Catal*. 1994;1:353–366.
114. Dumesic JA. Analyses of reaction schemes using De Donder relations. *J Catal*. 1999;185:496–505.
115. Shekhar M, Wang J, Lee W-S, Williams WD, Kim SM, Stach EA, Miller JT, Delgass WN, Ribeiro FH. Size and support effects for the water-gas shift catalysis over gold nanoparticles supported on model Al₂O₃ and TiO₂. *J Am Chem Soc*. 2012;134:4700–4708.
116. Shekhar M, Wang J, Lee W-S, Akatay MC, Stach EA, Delgass WN, Ribeiro FH. Counting Au catalytic sites for the water-gas shift reaction. *J Catal*. 2012;293:94–102.
117. Williams WD, Shekhar M, Lee W-S, Kispersky V, Delgass WN, Ribeiro FH, Kim SM, Stach EA, Miller JT, Allard LF. Metallic corner atoms in gold clusters supported on rutile are the dominant active site during water-gas shift catalysis. *J Am Chem Soc*. 2010;132:14018–14020.
118. Sanchez A, Abbet S, Heiz U, Schneider WD, Hakkinen H, Barnett RN, Landman U. When gold is not noble: nanoscale gold catalysts. *J Phys Chem A*. 1999;103:9573–9578.

119. Wang JL, Wang GH, Zhao JJ. Density-functional study of Au- n ($n=2-20$) clusters: lowest-energy structures and electronic properties. *Phys Rev B*. 2002;66:035418-1-035418-2.
120. Idrobo JC, Walkosz W, Yip SF, Oeguet S, Wang J, Jellinek J. Static polarizabilities and optical absorption spectra of gold clusters (Au- n , $n=2-14$ and 20) from first principles. *Phys Rev B*. 2007;76:205422-1-205422-12.
121. Ferrando R, Fortunelli A, Johnston RL. Searching for the optimum structures of alloy nanoclusters. *Phys Chem Chem Phys*. 2008;10:640-649.
122. Marx D, Hutter J. Ab initio molecular dynamics: theory and implementation. *Mod Methods Algorithm Quantum Chem*. 2000;301-449.
123. Zhai YP, Pierre D, Si R, Deng WL, Ferrin P, Nilekar AU, Peng GW, Herron JA, Bell DC, Saltsburg H, Mavrikakis M, Flytzani-Stephanopoulos M. Alkali-stabilized Pt-OH $_x$ species catalyze low-temperature water-gas shift reactions. *Science*. 2010;329:1633-1636.
124. Mager-Maury C, Chizallet C, Sautet P, Raybaud P. Platinum nanoclusters stabilized on gamma-alumina by chlorine used as a capping surface ligand: a density functional theory study. *ACS Catal*. 2012;2:1346-1357.
125. Fu Q, Saltsburg H, Flytzani-Stephanopoulos M. Active nonmetallic Au and Pt species on ceria-based water-gas shift catalysts. *Science*. 2003;301:935-938.
126. Guzman J, Gates BC. Oxidation states of gold in MgO-supported complexes and clusters: characterization by X-ray absorption spectroscopy and temperature-programmed oxidation and reduction. *J Phys Chem B*. 2003;107:2242-2248.
127. Guzman J, Gates BC. Simultaneous presence of cationic and reduced gold in functioning MgO-supported CO oxidation catalysts: evidence from X-ray absorption spectroscopy. *J Phys Chem B*. 2002;106:7659-7665.
128. Guzman J, Gates BC. Structure and reactivity of a mononuclear gold-complex catalyst supported on magnesium oxide. *Angew Chem Int Ed*. 2003;42:690-693.

Manuscript received Oct. 31, 2013, and revision received Jan. 28, 2014.